ORIGINAL ARTICLE

Fabrication of automotive titanium bipolar plates by uniform pressure electromagnetic incremental forming based on arc spiral coil

Qiangkun Wang[1] · Junrui Xu[1] · Yudong Zhao[1] · Shaobo Wang[1] · Yuanfeng Wang[1]

Abstract

Facing the forming requirements of large-sized automotive titanium bipolar plates (BPPs), a uniform pressure electromagnetic incremental forming (UP-EMIF) process was utilized. Corresponding simulation and analysis were conducted based on the designed arc spiral coil. Simulation revealed that during the forming process, electromagnetic forces on the coil wire tended to compress in radial direction, and the electromagnetic forces on the driver sheet transitioned from a wavy pattern to a uniform distribution. The maximum deformation velocity of the blank occurred at the bottom of the channel, reaching 195 m/s. The highest equivalent strain of the blank occurred in the rounded corner R region, which was prone to thinning of wall thickness. Based on these findings, UP-EMIF and traditional quasi-static drive rubber pad forming (QS-DRPF) experimental devices were developed, and a comparative study on the forming of 0.1-mm-thick automotive titanium BPPs was conducted. Research indicated that successful production of a titanium BPP measuring 485 mm × 195 mm was achieved using three consecutive discharges of 9 kV in each discharge region under the discharge capacitor of 100 μF, an acceleration distance of 2 mm, a coil overlap rate of 15%, and a 0.3-mm-thick Cu110 driver sheet. The depth of the channels was 0.4 mm (channel depth-to-width ratio of 0.53). Compared to traditional QS-DRPF, the 9 kV UP-EMIF reduced channel thinning effectively, with a maximum thinning rate of 18.2%, while simultaneously improving channel filling, with a maximum filling rate of 96.3%. This demonstrates the feasibility of UP-EMIF as a process for fabricating automotive titanium BPPs.

Keywords Titanium bipolar plate · Electromagnetic incremental forming · Arc spiral coil · Numerical simulation · Process parameter

1 Introduction

With the vigorous development of new energy vehicles, titanium bipolar plates (BPPs) are receiving increasing attention as core components of proton exchange membrane (PEM) fuel cells due to their high specific strength and corrosion resistance [1–3]. However, titanium exhibits poor formability and significant springback [4]. In traditional quasi-static forming techniques, problems such as shallow channel depth and large thinning in the rounded corner regions frequently occur [5, 6]. Mahabunphachai et al. [7] used cold stamping processes to fabricate Grade 1 and Grade 2 titanium BPPs under 200 kN pressure and 1 mm/s stamping velocity. The results showed shallow forming depths of 0.13 mm and 0.09

mm, respectively, with fracturing occurring in the Grade 2 titanium plate. Kim et al. [8] employed dynamic load stamping forming to produce Grade 5 titanium BPPs with a channel depth-to-width ratio of 0.252 (depth of 0.353 mm). Due to the low elongation rate of titanium, fractures occurred when the load exceeded 100 kN, leading the authors to conclude that cold stamping is not suitable for forming titanium BPPs. Jin [9] and Lee [10] utilized quasi-static drive rubber pad forming (QS-DRPF) techniques to fabricate Grade 5 titanium BPPs with a channel depth-to-width ratio of 0.3375 (depth of 0.27 mm) under forming conditions of 30 mm/s stamping velocity, 55 MPa pressing pressure, and a 10-mm-thick ShoreA20 rubber. However, rubber pad forming results in longer forming cycles and issues related to the lifespan of rubber pads. Therefore, a new and cost-effective forming method needs to be explored to improve the formability of titanium materials.

Electromagnetic forming (EMF) technology, with its non-contact high-speed characteristics, has the potential to

✉ Junrui Xu
xujunrui_hit@163.com

1 School of Materials Science and Engineering, Inner Mongolia University of Technology, Hohhot 010051, China

significantly enhance material formability, reduce spring-back, and suppress wrinkling [11], making it one of the most promising methods for addressing the challenges of titanium BPP forming [12, 13]. Kamal et al. [14] originally proposed the concept of uniform pressure coils (UPC) and used multiple discharges with a 0.13-mm-thick copper driver sheet to achieve the complete forming of SS301 stainless steel BPPs. However, this method required a high discharge energy of 19.7 kJ. Moreover, it might be challenging to form higher strength titanium plates using this level of energy. Wang et al. [15] employed UPC with a discharge energy of 8.0 kJ and a 0.15-mm-thick Cu110 copper sheet as the driver sheet to fabricate Grade 2 titanium BPPs with a channel depth-to-width ratio of 0.22, but the maximum average channel depth achieved was only 0.176 mm. Wu et al. [16] developed a new internal field UPC technique that achieved a maximum channel depth of 0.294 mm in TA1 BPPs under a discharge energy of 7.5 kJ, which has not yet reached the desired mold channel depth of 0.4 mm. Dong et al. [17] realized the formation of TA1 titanium BPPs with a channel depth-to-width ratio of 0.67 using a two-step stamping process with rigid molds wrapped in bidirectional Zylon fibers under the conditions of a discharge energy of 10.8 kJ and an acceleration distance of 4 mm in a vacuum chamber. Zhu et al. [18] proposed a hybrid forming method combining electromagnetic pulse forming and quasi-static forming (EMPB-QS), successfully producing 75-µm-thick pure titanium BPPs using a two-step stamping process with a 0.45 mm deep rigid mold. However, as a typical driving coil in the EMF field, UPC faces problems with coil strength [19, 20] and contact arcing [21, 22], making it difficult to form large-area and high-precision BPPs. To address these aforementioned issues, this study proposed a uniform pressure electromagnetic incremental forming (UP-EMIF) process using smaller uniform pressure coils and distributed multi-step forming achieved by moving internal primary coils to realize larger area forming. Based on this process, the application of UP-EMIF in the forming of TA1 titanium BPPs was systematically investigated, and the results were compared with measurements obtained using quasi-static (QS) forming methods.

The UP-EMIF process is a dynamic process involving the coupling of multiple physical fields, and numerical simulation analysis has become an efficient and cost-effective research approach. Imbert [23] and Oliveira [24] proposed a loosely-coupled numerical method to analyze the dynamic deformation behavior of thin plates during the EMF process, but this method did not consider the mutual coupling effect between the electromagnetic field and the structural field. To obtain more accurate simulation results, Yu et al. [25] further proposed the sequential coupling method, which divides the EMF process into multiple time steps and calculates the electromagnetic field and structural field separately in each

step. At the end of each step, the parameters are exchanged to prepare for the calculation of the next step. Cao et al. [26] performed numerical simulations of metal sheet EMF using the direct coupling method based on the COMSOL software. Xu et al. [27] conducted a loosely coupled study on the three-dimensional free bulging of uniform pressure coils using ANSYS software, unlike the axially symmetric characteristics exhibited by uniform pressure coils. In response to the issue of air mesh distortion, Cui et al. [28] utilized the ANSYS mesh adaption or remeshing technique to update the air mesh deformation according to the workpiece and established a three-dimensional sequentially coupled finite element model for uniform pressure coils to analyze their working principles and the distribution of magnetic forces on the sheet material. Kinsey et al. [29] first established a three-dimensional directly coupled finite element model for uniform pressure coils using LS-DYNA software, enabling more accurate analysis of workpiece deformation behavior. Cui et al. [30–33] first proposed a plate EMIF process based on flat coils for forming large curved parts. The grid updating during the EMIF process was achieved through ANSYS mesh remeshing technique, but required manually updating the air mesh based on the entire current curve in substeps. In this study, the LS-DYNA software was used to model the electromagnetic part and structural field using the boundary element method (BEM) and finite element method (FEM), respectively, without the need for an air mesh. The direct coupling of the UP-EMIF process was achieved through the transfer of internal variables.

2 Principle of UP-EMIF

The principle of UP-EMIF for the sheet is described in Fig. 1. The forming system consists of a pulse power supply system, UPC, square metal pieces, and forming molds. Inside the UPC, there is an arc spiral primary coil made of flat copper wire tightly wound around an epoxy plate; while on the outside, there is a slotted copper outer channel that maintains sliding contact with the primary coil. The metal sheet is in close electrical contact with the outer channel. By sequentially moving the primary coil to the predetermined positions on the large-sized metal sheet in the plane, when the switch K is closed, a pulsed current I_c is generated by the high-voltage capacitor C and flows into the primary coil. This induces a closed current I_w in the metal sheet and the inner wall of the outer channel. The opposing Lorentz force F_w arises between the primary current and the induced current, causing the metal sheet to impact the mold at high speed and acquire the desired shape. Compared to EMIF for the sheet based on a flat circular coil, the pressure on the metal sheet surface is uniformly distributed as a rectangular
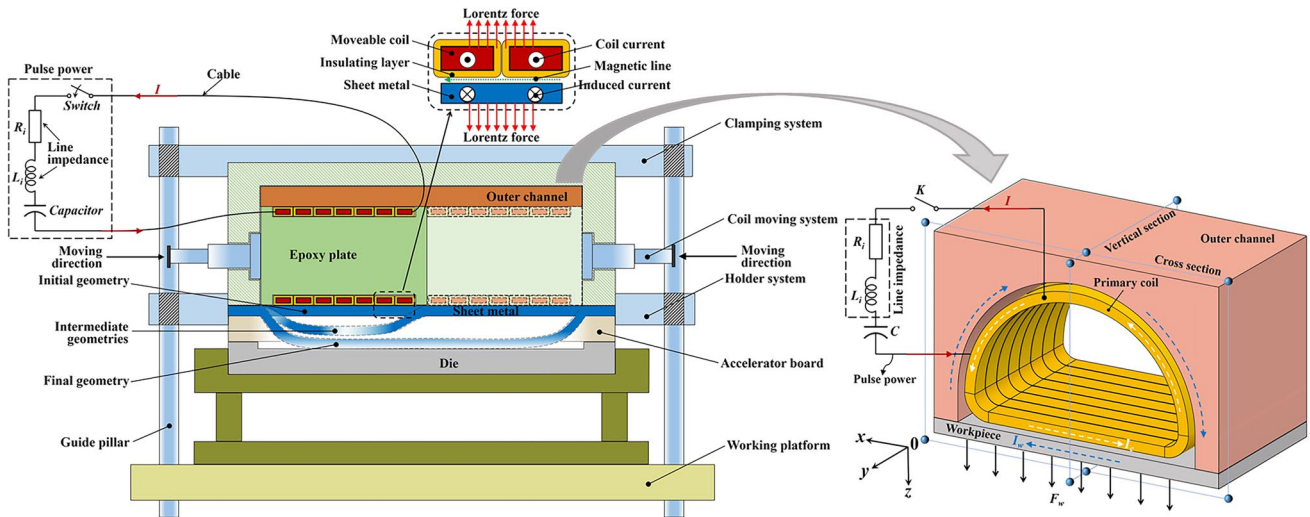
Fig. 1 The principle of uniform pressure electromagnetic incremental forming (UP-EMIF) for sheet metal based on arc spiral coils

shape, allowing the use of a small UPC and energy storage device to achieve high-precision shaping of automotive BPP.

3 Finite element model

3.1 Simulation process of UP-EMIF

The UP-EMIF process for sheet metal was analyzed using the finite element analysis software LS-DYNA. The entire simulation process can be divided into three modules: electromagnetic field module, structural field module, and coupling module. The electromagnetic field part is solved using the boundary element method without the need for an air mesh. The structural field part is modeled using the finite element method, and direct coupling is achieved through the transfer of internal variables. Fig. 2 shows the flowchart for simulating the UP-EMIF process. Let n be the number of coil movements. When the coil is in a fixed position, let T_0 be the deformation time of the plate. The coil movement time is denoted as t'. Therefore, the total time for the UP-EMIF process is $T = (i + 1) \times T_0 + i \times t'$.

3.2 Geometry of UP-EMIF system

The geometry of the UP-EMIF system is depicted in Fig. 3. The primary coil has a length of 197 mm and a height of 93.5 mm, with a wire cross-sectional area of 2×5 mm and a turn spacing of 3 mm. The outer channel has a maximum thickness of 15 mm. The gap between the primary coil and

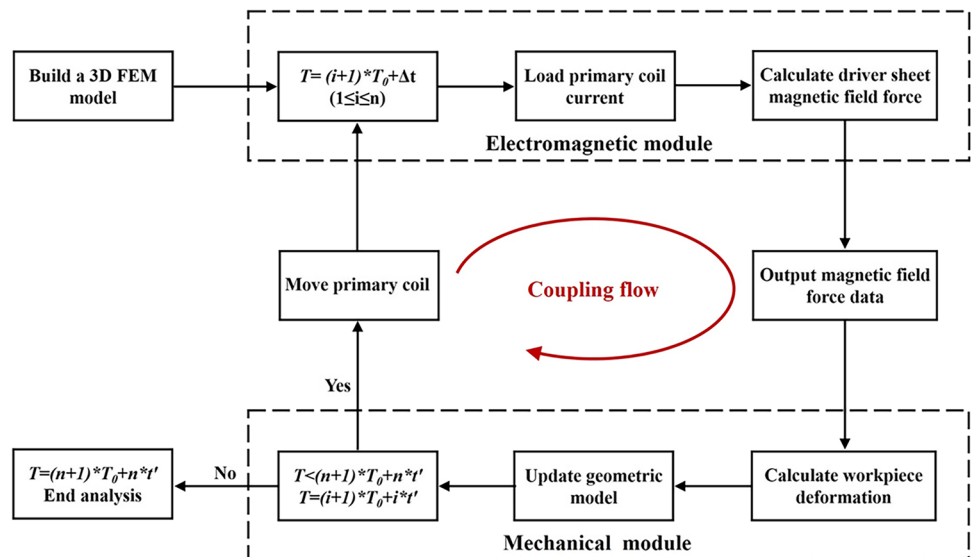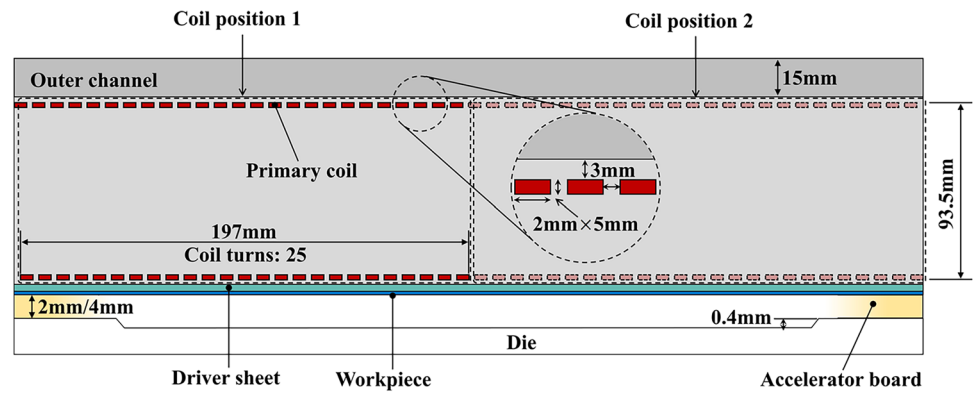**Fig. 2** Flowchart of sequential coupling algorithm for UP-EMIF

Fig. 3 Geometry diagram of UP-EMIF titanium BPP

the driver sheet and outer channel is 3 mm. Accelerator boards with thicknesses of 2 mm and 4 mm are selected to provide acceleration distance for the workpiece. The workpiece is composed of TA1 titanium plate, which has a thickness of 0.1 mm and dimensions of 166×400 mm. Due to the low electrical conductivity of titanium, the plate cannot generate sufficient induced current in the magnetic field, thereby resulting in inadequate electromagnetic force. Typically, driver sheets with high electrical conductivity are employed for driving, and Cu110 copper sheets with thicknesses of 0.2 mm and 0.3 mm are adopted. Fig. 4 illustrates the structural dimensions of the die. The die flow field consists of 5 arrays of straight channels with a depth-to-width ratio of 0.53 (with a channel depth of 0.4 mm and a channel width of 0.75 mm), primarily investigating the influence in the rolling direction.

3.3 Discharge path planning

Figure 5 illustrates the planning of the coil discharge path. Under low discharge energy, the coil is set to discharge from left to right along the BPP flow channel, forming the first discharge step, referred to as the first discharge. Then, it continues to discharge in the opposite direction, from right to left, forming the second discharge step, referred to as the second discharge. This process continues until the completion of the workpiece forming. Throughout the process, the coil undergoes multiple discharges at the same position. To investigate the influence of coil position on the forming results at each shaping stage, the concept of coil overlap ratio δ is introduced, which represents the ratio of the overlapped portion between the primary coil and the previous forming position to the length of the primary coil.
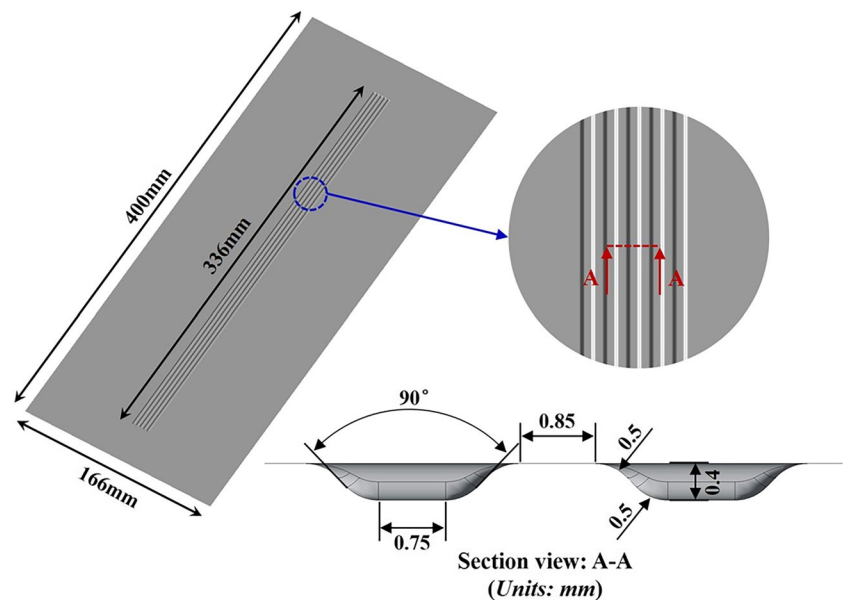
Fig. 4 Geometry of the die

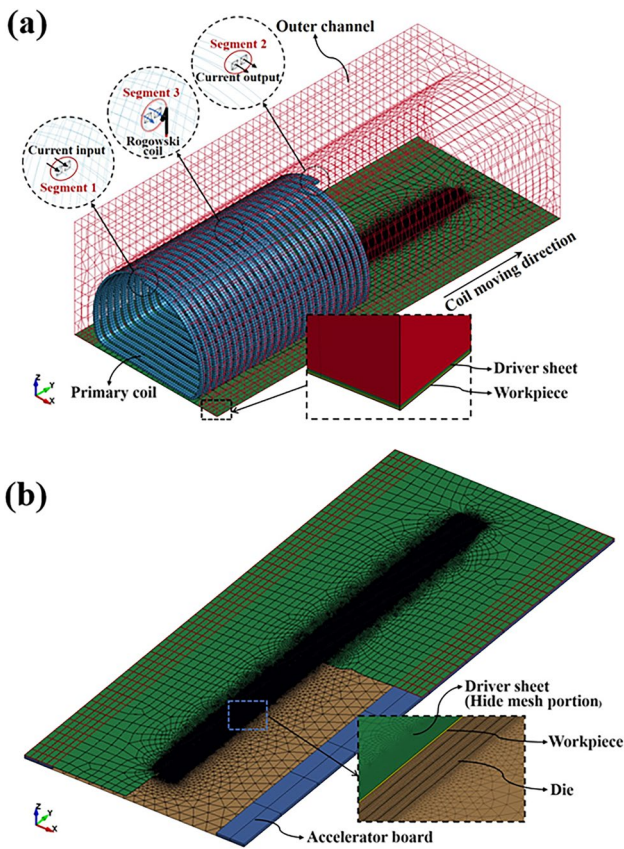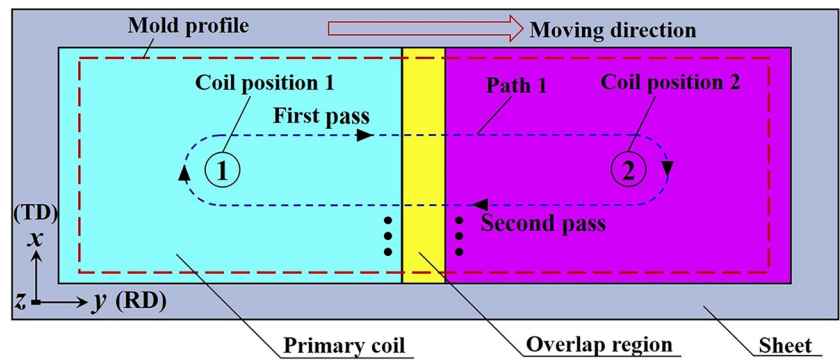**Fig. 5** Discharge path planning of the coil

Fig. 6 Finite element model of UP-EMIF titanium BPP. **a** Electromagnetic field model of the upper part; **b** deformation field model of the lower part

3.4 Coupled field model

Figure 6 depicts the finite element model of the UP-EMIF titanium BPP. To ensure the proper formation and continuity of the induced current loop between the driver sheet and the outer channel, the mesh nodes on the contact surface of the outer channel and the driver sheet are merged. The mesh is refined for the coil wires, driver sheet thickness direction, and inner wall of the outer channel to accurately capture the skin effect of the current. The deformation region of the driver sheet and workpiece is meshed with refinement to accurately capture the bending deformation of the sheet metal. Table 1 presents the material property settings and mesh division in the forming system. The primary coil, outer channel, accelerator board, and die are defined as rigid bodies, with the mass density, elastic modulus, and Poisson's ratio defined using the "*MAT_RIGID" keyword and the "RO, E, and PR" options. The electromagnetic material type and initial electrical conductivity of the material are defined using the "MTYPE and SIGMA" options in the "*EM_MAT_001" keyword.

The Cu110 driver sheet and TA1 workpiece are defined using the keyword "*MAT_JOHNSON_COOK" to represent the Johnson-Cook material model. Equation (1) is employed to describe the constitutive relationship of the sheet metal under high strain rates, considering strain hardening, strain rate hardening, and thermal softening of the material.

Table 1 Material property settings and mesh division

Material	RO (kg/m³)	E (Pa)	PR	MTYPE	SIGMA(S/m)	MESHING
Cu110 primary coil	8.98×10^3	1.37×10^{11}	0.31	2	5.81×10^7	SWEEP
Cu230 outer channel	8.53×10^3	1.00×10^{11}	0.33	4	1.52×10^7	SWEEP
Rubber accelerator board	1.00×10^3	6.10×10^6	0.49	1	—	SWEEP
45# steel die	7.89×10^3	2.09×10^{11}	0.27	1	—	FREE
C110 driver sheet	8.89×10^3	1.37×10^{11}	0.31	4	5.81×10^7	SWEEP
TA1 workpiece	4.51×10^3	1.05×10^{11}	0.33	4	1.80×10^6	SWEEP

$$\sigma_0 = \left(A + B \cdot \dot{\varepsilon}^n\right)\left(1 + C \cdot \ln\frac{\dot{\varepsilon}}{\dot{\varepsilon}_0}\right)\left[1 - \left(\frac{T - T_r}{T_m - T_r}\right)^m\right] \quad (1)$$

In the Eq. (1), σ_0 represents the equivalent yield strength; ε denotes the equivalent strain; $\dot{\varepsilon}$ and $\dot{\varepsilon}_0$ represent the equivalent plastic strain rate and reference strain rate, respectively; A is the yield stress at room temperature; B and n are the strain hardening parameters and strain hardening exponent, respectively; C is the strain rate hardening coefficient; m is the thermal softening coefficient; T_r and T_m are the room temperature and material melting temperature, respectively. The constitutive model parameters for Cu110 and TA1 are shown in Table 2 [34, 35].

To avoid initial contact penetration, the contacting components are set with "Automatic Surface to Surface" surface contact. The springback effect generated after the workpiece contacts the die is defined using the keyword "*SPRING-BACK." The primary coil retains translational freedom in the Y direction, while the outer channel is fixed. The clamping force on the workpiece is provided by the outer channel, eliminating the need for a clamping system.

The EM eddy current solver is activated by defining the option "EMSOL=1" in the keyword "*EM_CONTROL." The magnetic field boundary conditions are defined by the option "BTYPE=9" in the keyword "*EM_BOUNDARY," excluding the bottom surface and side boundaries of the slab to simplify the calculation. The electromagnetic contact between the outer channel and the driver sheet is defined using the keywords "*EM_CONTACT" and "*EM_CONTACT_RESISTANCE," allowing induced currents to flow from one to another and calculating the contact resistance of the defined EM contact points. The circuit parameters are defined in the keyword "*EM_CIRCUIT" with the option "CIRCTYP=1," applying current waveforms at the ends of the conductor, where the current flows in through "SSIDVIN" and out through "SSIDVOUT." The output of current data flowing through the surface segment group is measured using the Rogowsky coil, defined in the keyword "*EM_CIRCUIT_ROGO." After completing the parameter settings for the structural and electromagnetic fields mentioned above, the process of building the sequential coupling model is essentially completed.

To avoid workpiece oscillation and rebound in the second half of the first rising period during discharge, as shown in Fig. 7a, the time node at which the 0.4-mm channel depth is reached is taken as the end time of each discharge step, resulting in a fitted current waveform for a single incremental forming process, as shown in Fig. 7b. According to the simulated time and discharge path, the measured and fitted current variations are loaded as boundary conditions on the starting surface segment group of the coil wire to achieve multi-step UP-EMIF.

4 Experimental procedure

### 4.1 Coil design and manufacturing process

To design a UPC for forming automotive titanium BPP and ensure the dimensions of the UPC structure are reasonable, the size of the mold needs to be determined first. The BPP mold used in this study has a multi-channel parallel wavy flow field, with a total of 20 channels. The channel depth is 0.4 mm, and the channel width is 0.75 mm (the aspect ratio of depth to width is 0.53). The area of the flow field is 335 mm × 82 mm, and the total area of the mold cavity is 408 mm × 102 mm, as shown in Fig. 8a.

In order to generate a sufficiently large electromagnetic force for deformation, it is important to design the coil. However, due to the limitations of the mold size and considering the convenience of setting up the experimental platform and performing discharge operations, a split-winding type UPC is adopted. It is constructed using double glass-fiber–covered flat copper wire on the inside and double-layer

Table 2 J-C constitutive model parameters for Cu110 and TA1

Material	A (MPa)	B (MPa)	C	n	m	T_{room} (K)	T_{melt} (K)	$\dot{\varepsilon}_0$ (s^{-1})
Cu110	89.63	291.64	0.025	0.31	1.09	27	1200	1.0
TA1	215	380	0.0302	0.18	0.55	27	1950	1.0

Fig. 7 Under single pass discharge: **a** displacement of the workpiece and **b** current curve of the primary coil loading
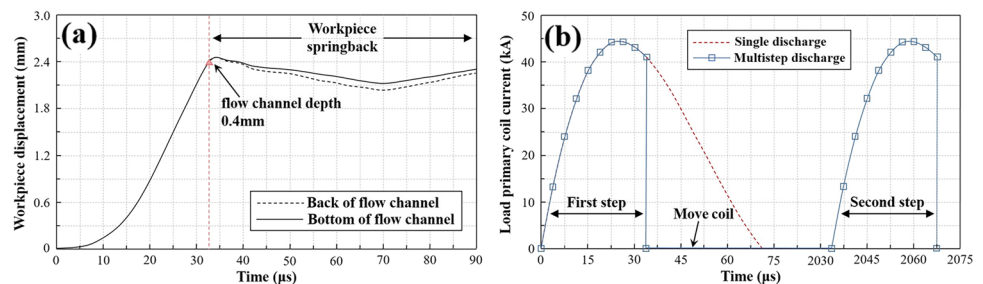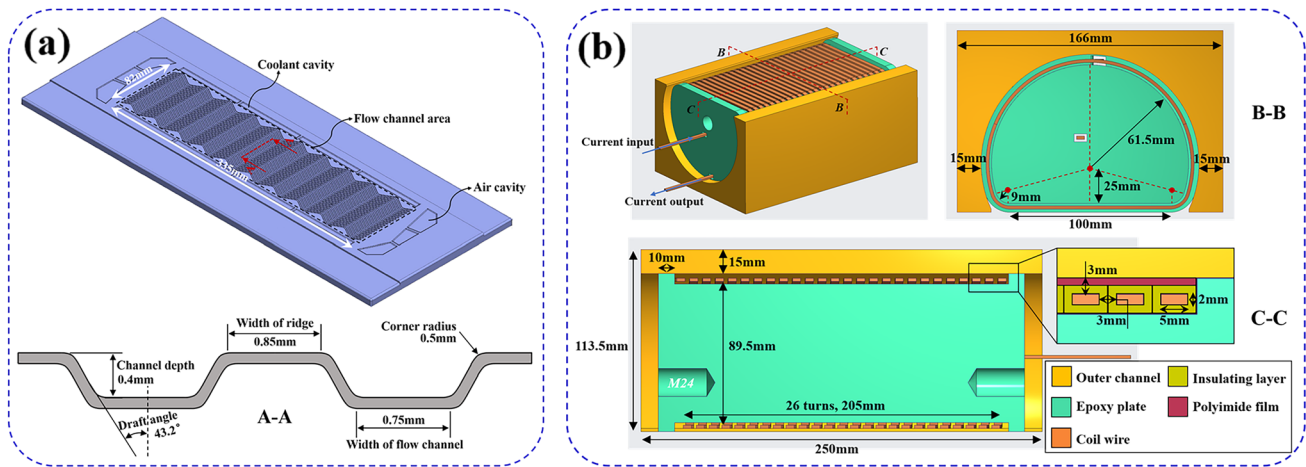
Fig. 8 **a** BPP mold; **b** split winding UPC

polyimide film on the outside. The epoxy plate at the center of the coil provides support for the coil wires. The geometric structure of the UPC is illustrated in Fig. 8b.

For the selection of coil wire dimensions, the wire cross-sectional area is chosen as 2 mm × 5 mm, with a total of 26 turns for the coil wire and a spacing of 3 mm between turns. When the wire insulation layer has a thickness of 1.5 mm, the length of the primary coil in the direction perpendicular to the cross-section is 208 mm. For the height of the primary coil, a net height of 93.5 mm is chosen (with an internal height of 89.5 mm for the primary coil). For the air gaps between the primary and secondary sides of the coil, the net distance between the curved side of the coil wire and the outer channel is maintained at 3 mm, while the net distance between the lower surface side of the coil wire and the Cu110 driver sheet is maintained at 2 mm. Reinforce along the winding direction of the wire with a double-layer polyimide film of approximately 0.4 mm thickness, resulting in a total height of the primary coil of approximately 98.5 mm after including the polyimide film, with an air gap of approximately 0 mm between the primary and secondary sides of the coil. To reduce the electrical contact area between the outer channel and the driver sheet and alleviate arc problems, the wall thickness of the outer channel should be kept as small as possible while ensuring strength. Therefore, a minimum wall thickness of 15 mm is chosen for the outer channel. To reduce the impact of coil end effects, the primary coil is positioned with approximately 15 mm clearance from both ends of the outer channel, ensuring that the primary coil is centered within the outer channel. Therefore, the final total height of the UPC is 113.5 mm, with a total length of 250 mm and a total width of 166 mm.

Figure 9 illustrates the manufacturing process of the coil. Firstly, high-strength epoxy plate is chosen as the support frame for the coil, providing insulation as well. Next, the

wire grooves and channels on the epoxy plate are machined using CNC technology, as shown in Fig. 9a. Then, the 2 × 5 mm² copper wire is manually wound according to the groove shape, as shown in Fig. 9b. The shape of the winding coil includes a spiral with an arc shape and two straight sections, with the two straight sections subsequently connected to the EMF device to form a current loop. For the convenience of winding the coil, a simple manual coil winding device is designed, as shown in Fig. 9c. The coil epoxy plate is fixed on the workbench, and during winding, the copper wire is guided into the pre-set grooves to complete the coil winding. Fig. 9d shows the assembly result of the epoxy plate and the coil winding. Due to the winding wire being embedded in the epoxy plate, there is a small gap. To prevent relative movement between the winding wire and the outer channel during the forming process, the assembled coil is externally encapsulated with a 0.4-mm-thick polyimide film. Thus, a working coil suitable for UP-EMIF experiments is obtained, as shown in Fig. 9e. Figure 9f depicts the actual schematic of the assembly result between the coil and the epoxy plate.

4.2 UP-EMIF experiment

The experimental setup for EMIF titanium BPP based on UPC is shown in Fig. 10a, consisting of a device frame and a forming section. The device frame is equipped with AA1060 upper and lower pressure plates as well as side support plates, providing positioning and support functions. The installation schematic and physical image of the forming section are shown in Fig. 10a and b, including Cu230 outer channel, Cu110 coil wire, FR4 epoxy plate, Cu110 driver sheet, and AA1060 edge pressing block. The forming coil is placed inside the outer channel, while the workpiece and driver sheet are placed above the BPP mold and assembled inside the device frame. To avoid voltage breakdown, the

Fig. 9 Coil manufacturing process: **a** grooving on epoxy plate using CNC machining; **b** wire winding; **c** manual winding coil device; **d** assembly after wire winding; **e** encapsulation with 0.4-mm-thick polyimide film; **f** actual coil before encapsulation
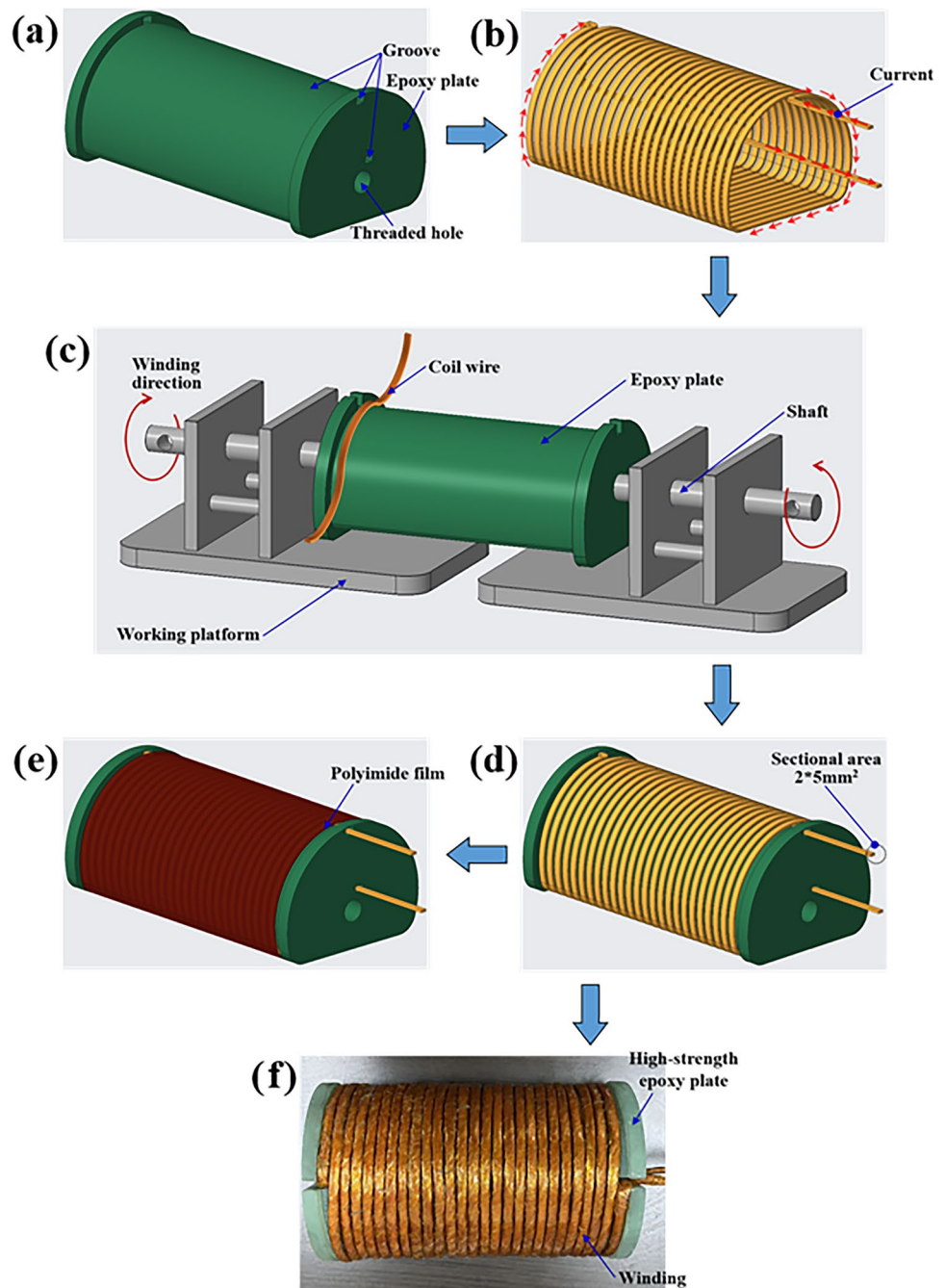
surrounding sidewalls of the outer channel are insulated with 3240 epoxy plate. The rubber accelerator board is placed between the concave mold sides and the metal sheet to reduce arc problems and achieve higher impact speeds. The EMF-20 equipment is selected, and its device parameters are shown in Table 3.

To reduce electrical contact issues before the discharge experiment, the outer channel area in contact with the driver sheet is coated with conductive silver adhesive, as shown in Fig. 10b. The discharge current variation was measured using a Rogowski coil, and Fig. 10c shows the fitted current

curves obtained at discharge energies of 4.05 kJ, 7.2 kJ, and 11.25 kJ. Uniaxial tensile tests were performed on 0.1-mm-thick TA1 ultra-thin titanium strips in the annealed state at 750 °C using an Instron 5980 universal testing machine. The uniaxial tensile curve at a strain rate of 6.67×10 s^{-4} is obtained, as shown in Fig. 11.

4.3 QS experiment

To compare with the traditional QS-DRPF process, Fig. 12 shows the experimental setup for traditional QS-DRPF of

Fig. 10 **a** UP-EMIF experimental setup; **b** physical diagram of the die and coil; **c** measured coil current variation curve
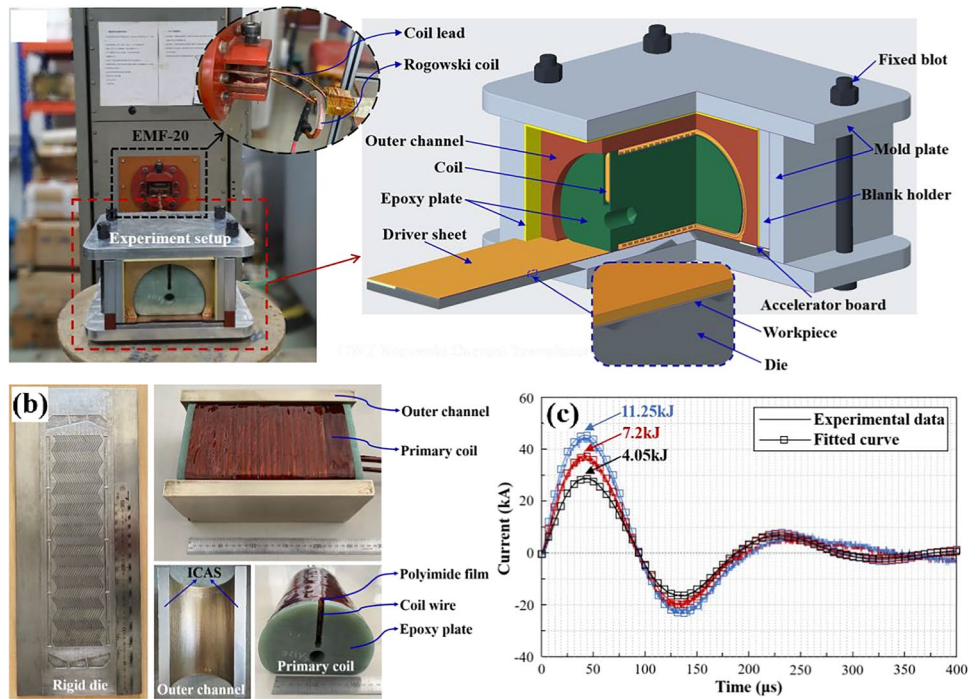
Table 3 Parameters of EMF equipment

Equipment model	Rated voltage (kV)	Energy storage capacitor (μF)	Maximum charging (kJ)	Line inductance (μH)	Line resistance (mΩ)
EMF-20	20	100	20	0.6	3
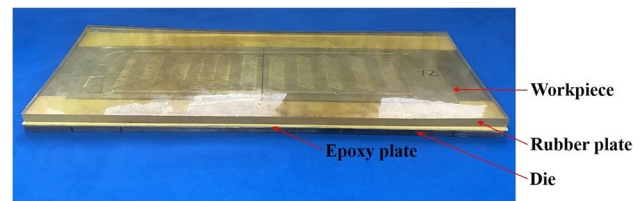
Fig. 12 Traditional QS-DRPF experimental setup
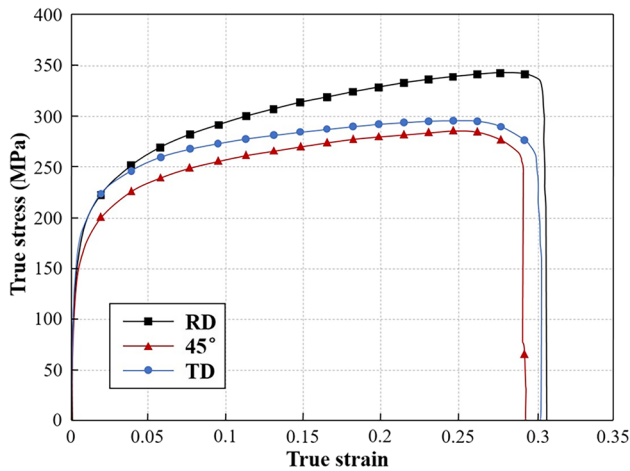
Fig. 11 True stress-strain curve at a strain rate of $6.67 \times 10 \text{ s}^{-4}$

titanium BPP. The forming section includes the 45# steel mold, rubber pad sheet, and TA1 workpiece. The Tianduan 300-1500×1500 hydraulic press is selected, and its equipment parameters are shown in Table 4. Before forming, the

assembled experimental setup is placed flat on the press table without edge pressing, and the downward tonnage of the slide is set. During the forming process, the descent speed of the slide and the strain rate are controlled at 0.02 mm/s and $(6\sim7) \times 10 \text{ s}^{-4}$, respectively.

5 Results and discussion

5.1 Analysis of electromagnetic characteristics

5.1.1 Current distribution of UPC

The electromagnetic characteristics of arc UPC and the dynamic response process of the metal sheet are analyzed under the conditions of discharge capacitor of 100 μF, discharge voltage of 15 kV, acceleration distance of 2 mm, and coil overlap rate of 0%.

Figure 13 shows the current distribution of the arc UPC. The induced current in the driver sheet and outer channel

Table 4 Parameters of traditional QS-DRPF equipment

Equipment model	Maximum nominal force (kN)	Slider working speed (mm/s)	Worktable area (mm)	Rubber dimension (mm)	Rubber hardness (HA)
Tianduan 300-1500×1500	5000	0.002~15	1500×1500	$485 \times 195 \times 10$	70
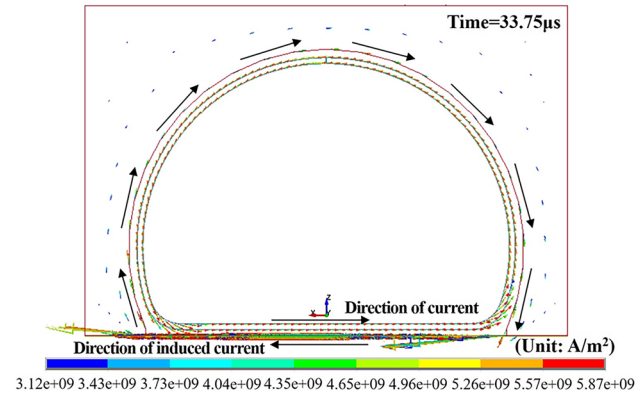
Fig. 13 Overall distribution of current density vector in UPC

the center of the coil wire towards both sides in the width direction, and the current is larger near the driver sheet side in the thickness direction of the coil wire. Fig. 15a shows the vector distribution of current density in the outer channel. The current flows from the inner wall of the outer channel into the driver sheet. Fig. 15b shows the surface current distribution map of the outer channel. The current in the outer channel mainly concentrates on the inner wall, and the distribution is uniform in the position opposite to the coil wire. Fig. 16a shows the vector distribution of current density in the driver sheet. The current in the driver sheet flows in the TD direction, and the current density distribution in the deformation area is uniform, which is consistent with the surface current distribution pattern shown in Fig. 16b.

5.1.2 Magnetic flux density and magnetic pressure distribution

Due to the difficulty of experimentally determining the magnetic field, the finite element method is used to analyze the magnetic induction intensity and magnetic pressure to evaluate the variation of the magnetic field. Fig. 17 shows the vector distribution of magnetic flux density in the primary coil

forms a closed loop, completely enveloping the primary coil, avoiding coil magnetic field loss, and improving the utilization of magnetic field energy. Fig. 14a shows the vector distribution of current density in the primary coil. Current density concentration occurs at the input and output positions. Fig. 14b shows the surface current distribution map of the primary coil. The current decreases gradually from

Fig. 14 3D current distribution of the primary coil: **a** current density vector distribution; **b** surface current nephogram

Fig. 15 3D current distribution of the outer channel: **a** current density vector distribution; **b** surface current nephogram

Fig. 16 3D current distribution of the driver sheet: **a** current density vector distribution; **b** surface current nephogram
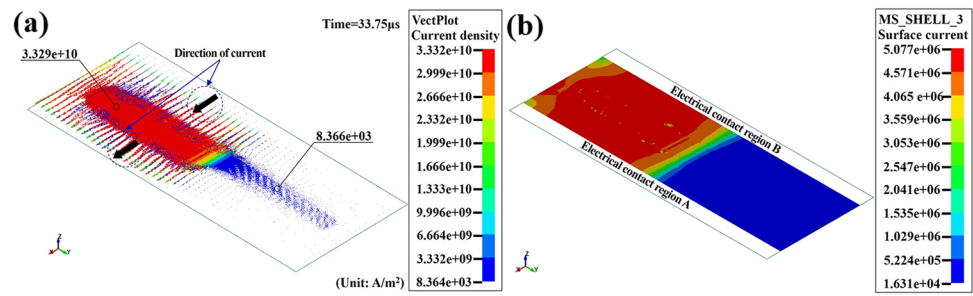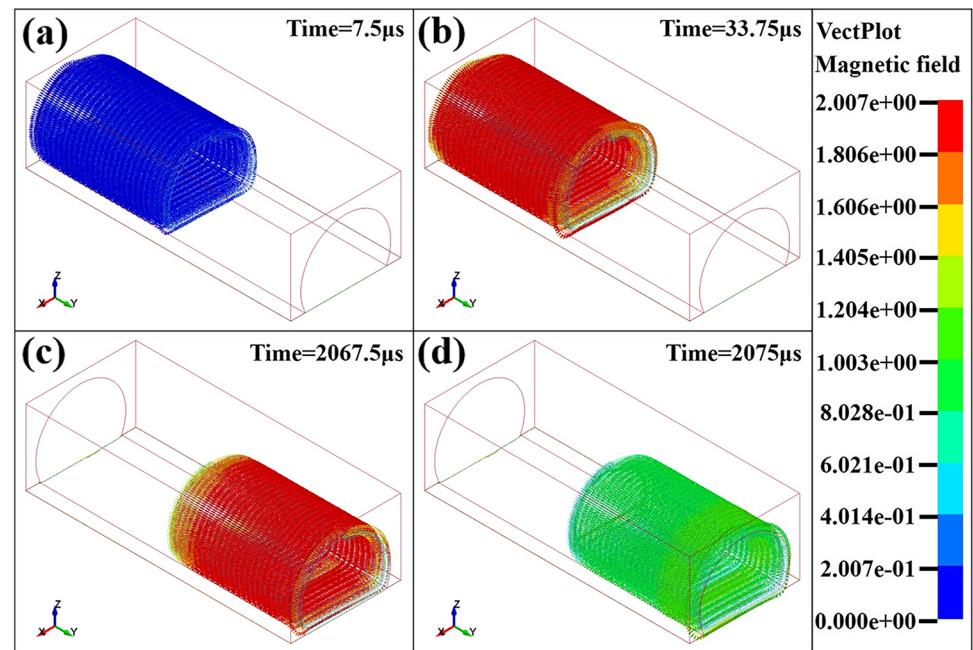

Fig. 17 Vector distribution of magnetic flux density in the primary coil over time: **a** 7.5 μs; **b** 33.75 μs; **c** 2067.5 μs; **d** 2075 μs

at different time points. Due to the closed loop formed by the plate and the outer channel, the magnetic flux density in the primary coil is distributed uniformly. As time increases, the maximum magnetic flux density occurs at each step of the current peak. Fig. 18 shows the distribution nephogram of magnetic flux density in the driver sheet at different time points. The magnetic flux density in the deformation region of the driver sheet is uniformly distributed. The quantitative analysis of the magnetic pressure on the driver sheet is shown in Fig. 19, where 9 typical points are selected along the RD and TD directions on the surface of the deformation region of the driver sheet. It can be observed that, except for the coil ends and overlapping regions, the peak magnetic pressure in the deformation region coincides, confirming the reliability of the arc UPC in providing uniform pressure.

5.1.3 Electromagnetic forces distribution

Figures 20 and 21 present the distribution nephogram and vector of electromagnetic forces in the primary coil. The electromagnetic forces acting on the wires all develop towards the inner radius. To understand the direction of electromagnetic forces on the straight section of the wire, 6-turn wires from the region of uniform electromagnetic forces, denoted as region B, are selected. In the direction of wire thickness, each turn of the wire experiences electromagnetic forces directed downward along the Z-axis, while in the direction of wire width, each turn of the wire experiences electromagnetic forces inclined at a small angle inward with respect to the Z-axis, resulting in a tendency for compression of the wire. According to the work reported by Cui et al. [28], the protrusion at the bottom of the racetrack-shaped UPC is due to the stronger electromagnetic forces in the upper region of the coil. Therefore, the arc-shaped UPC is less likely to cause ballooning failure at the bottom of the coil. Fig. 22a displays the nephogram of electromagnetic forces in the outer channel. The electromagnetic forces primarily act on the top and bottom inner walls of the outer channel. Fig. 22b shows the vector distribution of electromagnetic forces in the outer

Fig. 18 Nephogram of magnetic flux density in the driver sheet over time: **a** 11.25 μs; **b** 26.25 μs; **c** 2060 μs; **d** 2075 μs
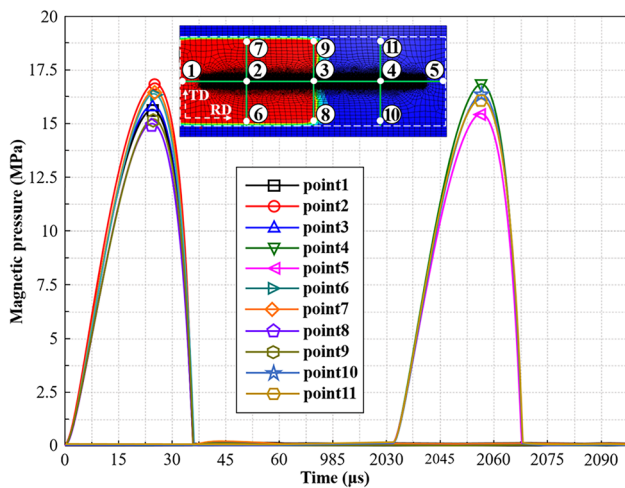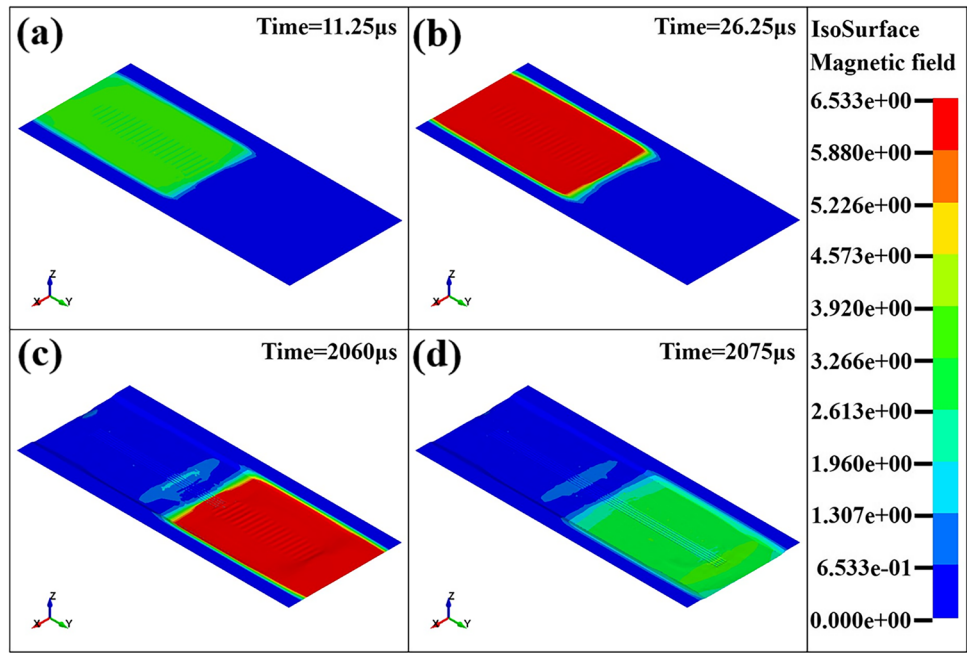

Fig. 19 Variation of magnetic pressure at different positions on the surface of the driver sheet
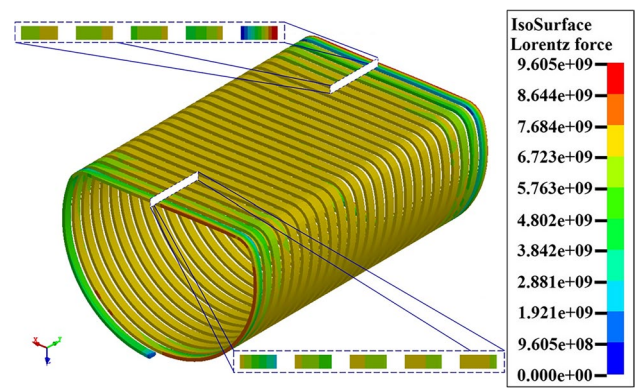

Fig. 20 Distribution nephogram of electromagnetic forces on the primary coil

5.2 Analysis of deformation characteristics

5.2.1 Analysis of displacement field

channel. The electromagnetic force at the bottom of the outer channel is the largest and develops in a direction inclined at a small angle with respect to the Z-axis, exhibiting a tendency to repel the driver sheet. This is the main cause of arc generation during the experimental process. Fig. 23 displays the vectors of electromagnetic forces acting on the two discharge regions in the driver sheet along the TD direction, based on the ZOY coordinate plane, at different time points. The electromagnetic forces on the driver sheet exhibit a continuous sinusoidal distribution along the wire width, with a direction opposite to that of the electromagnetic forces in the primary coil.

Due to the difficulty of experimentally determining the dynamic response process of metal sheets, the finite element method is used to analyze the changes in velocity, displacement, and stress-strain during the forming process, in order to evaluate the characteristics of the forming process. Fig. 24a shows the displacement contour of the workpiece. With an acceleration distance of 2 mm, only 11.25 kJ of discharge energy is required for the complete forming of titanium BPP, with a channel depth of 0.4 mm. To observe the displacement variation with time at typical positions on the workpiece, paths ab, cd, and

Fig. 21 Vector distribution of electromagnetic forces on the primary coil: **a** overall vector distribution; **b** vector distribution in the uniform electromagnetic force region B
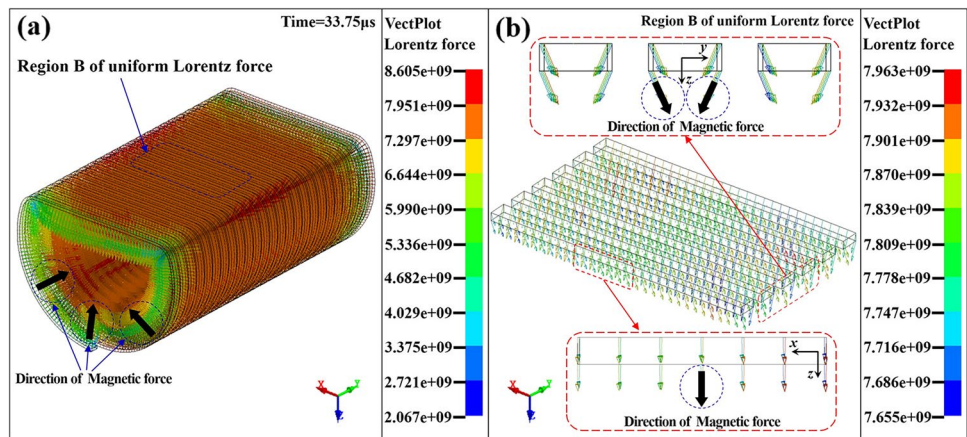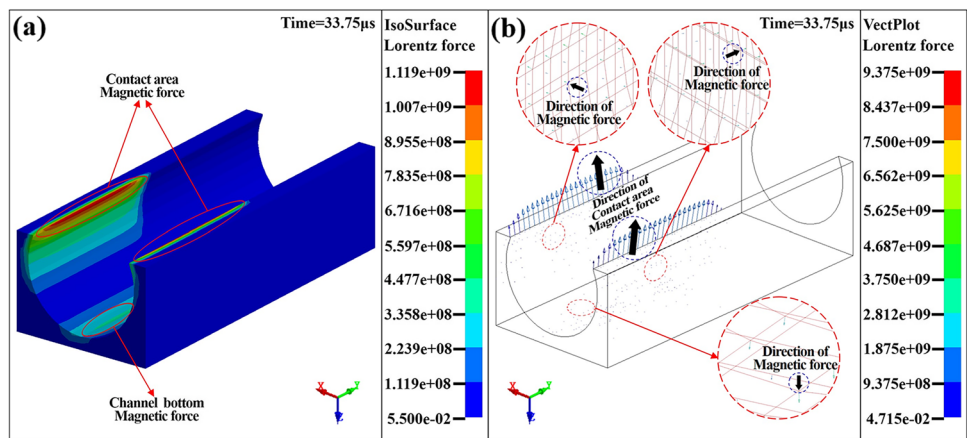

Fig. 22 Distribution of electromagnetic forces on the outer channel: **a** distribution nephogram of electromagnetic forces; **b** vector distribution of electromagnetic forces

ef are selected along the TD and RD directions of the workpiece. In the central single-channel region α along the groove bottom to the ridge in the ab path, elements A, B, C, and D are selected. The positions of the selected elements and their displacement-time curves are shown in Fig. 24b. After 37.5 μs, typical elements A, B, C, and D come into contact with the surface of the mold, and their displacements remain stable without any significant rebound phenomenon.

Figure 25 shows the deformation profiles of various nodes of the sheet at different time points in the TD and RD directions, from the start of acceleration to the collision with the mold, with a total duration of approximately 41.25 μs. At 33.75 μs, due to the relatively small electromagnetic force between the coil wires, the workpiece generates an uneven wave-like displacement just before colliding with the mold. Benefiting from the uniform electromagnetic force exerted by the arc UPC, at time points 41.25 μs and 2075 μs, the sheet undergoes uniform plastic deformation, with a channel depth of 0.4 mm achieved at all five straight channels and a channel filling rate exceeding 95%. Additionally, the deformation of the workpiece in the coil overlap region is relatively small.

5.2.2 Analysis of velocity field

Dong et al. [17] discovered that there will be a process of rebound and repeated oscillation after the titanium sheet impacts the mold. Excessive rebound will inevitably impact the channel depth of titanium BPP and increase the warping of the sheet. Therefore, to eliminate this situation, it is essential to ensure the presence of a significant downward velocity vector on the sheet during the impact process. Fig. 26 shows the velocity distribution contour of the titanium plate during the forming process. Prior to colliding with the mold (at 22.5 μs and 2052.5 μs), the titanium plate experiences uniform impact force, resulting in a relatively uniform distribution of forming velocity and a relatively smooth surface. After the completion of the collision (at 48.75 μs and 2075 μs), the central part of the titanium plate experiences a rebound phenomenon, resulting in slight wrinkling and the presence of raised burrs on both sides of the titanium BPP. Extracting the forming regions of the titanium plate corresponding to the 5 array channels, Fig. 27 shows the distribution of velocity vectors in the titanium plate during the forming process. At 26.25 μs, the titanium plate maintains a

Fig. 23 The electromagnetic forces on the two discharge regions of driver sheet at different time points: **a** 26.25 μs; **b** 41.25 μs; **c** 52.5 μs; **d** 2075 μs
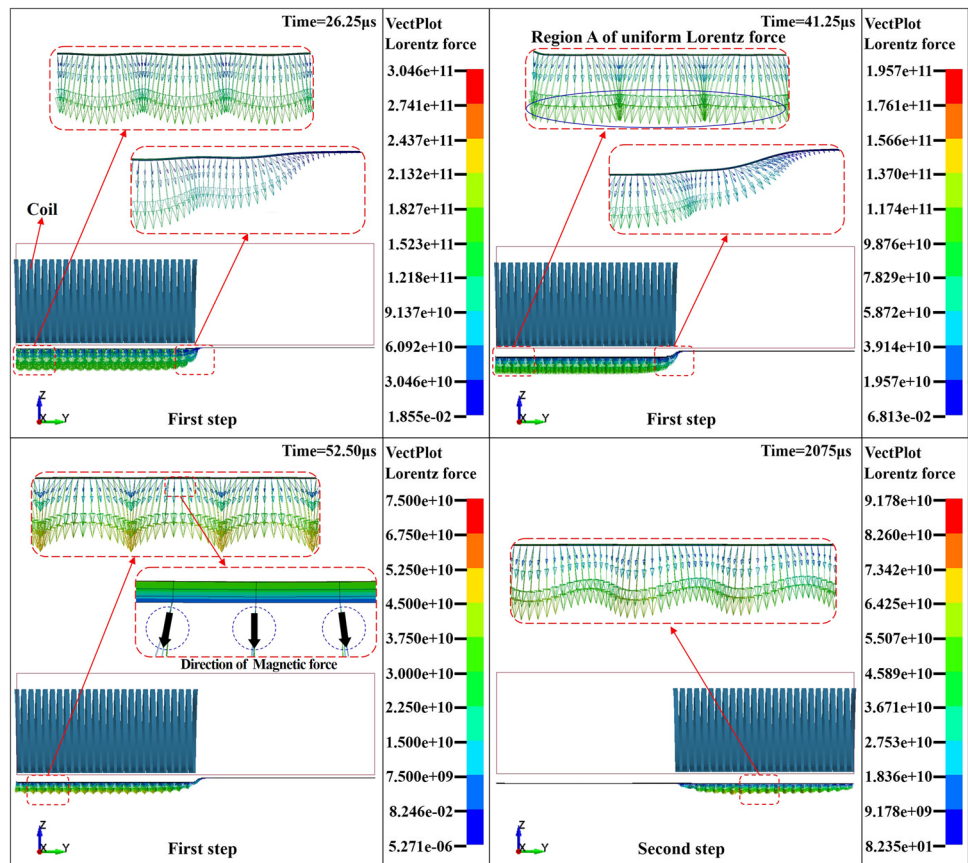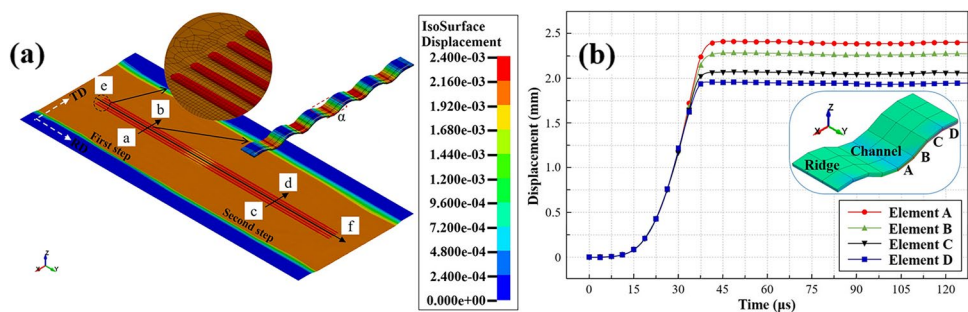

Fig. 24 **a** Displacement nephogram of the workpiece; **b** displacement-time curve of a typical element in the single-channel region α

downward velocity along the Z-axis. By 37.5 μs, after completing the collision with the mold, the deformation velocity propagates upward, resulting in a slight "negative" strain rate and exhibiting oscillatory rebound of the titanium plate. Fig. 28 shows the typical element velocity variation with time in the single-channel region α. Prior to colliding with the mold, the velocities of the individual elements are consistent with the displacements, and the velocity of the titanium plate increases almost linearly. After colliding with the mold (around 37.5 μs), the velocity of element A located at the bottom of the groove reaches its maximum value of 195 m/s.

5.2.3 Analysis of stress and strain

Figure 29 shows the equivalent strain nephogram of the titanium plate at different time intervals. When the first discharge region is formed (41.25 μs), the equivalent strain exhibits a linear distribution with a value of 0.103. When the second discharge region is formed (2075 μs), the equivalent strain of the titanium plate in the coil overlap region is relatively small, only 0.04. The temporal variation of the equivalent strain of the typical element in the single channel region α is shown in Fig. 30. The equivalent strain in elements A and B is noticeably higher compared

Fig. 25 Deformation profiles of various nodes on the sheet at different time points, **a** in the TD direction; **b** in the RD direction
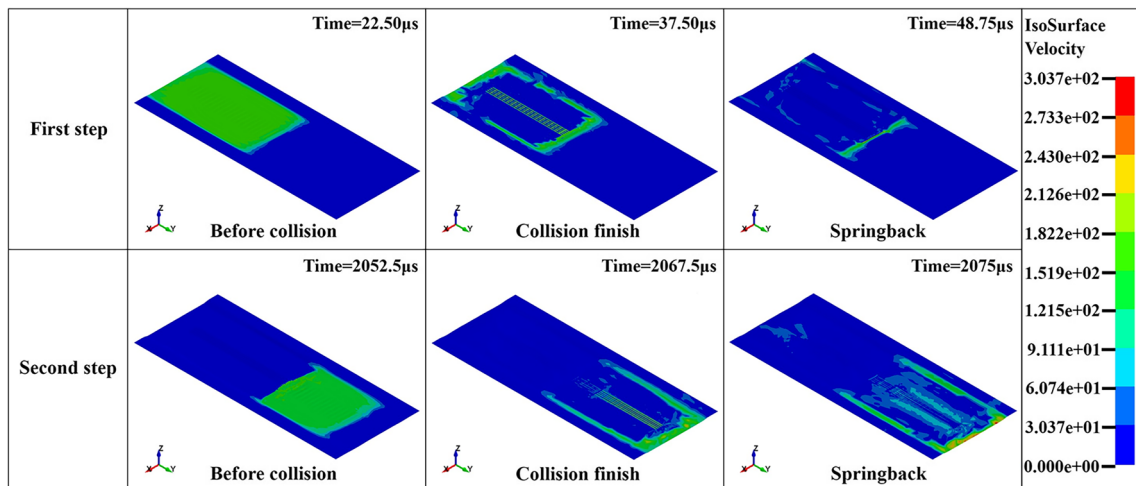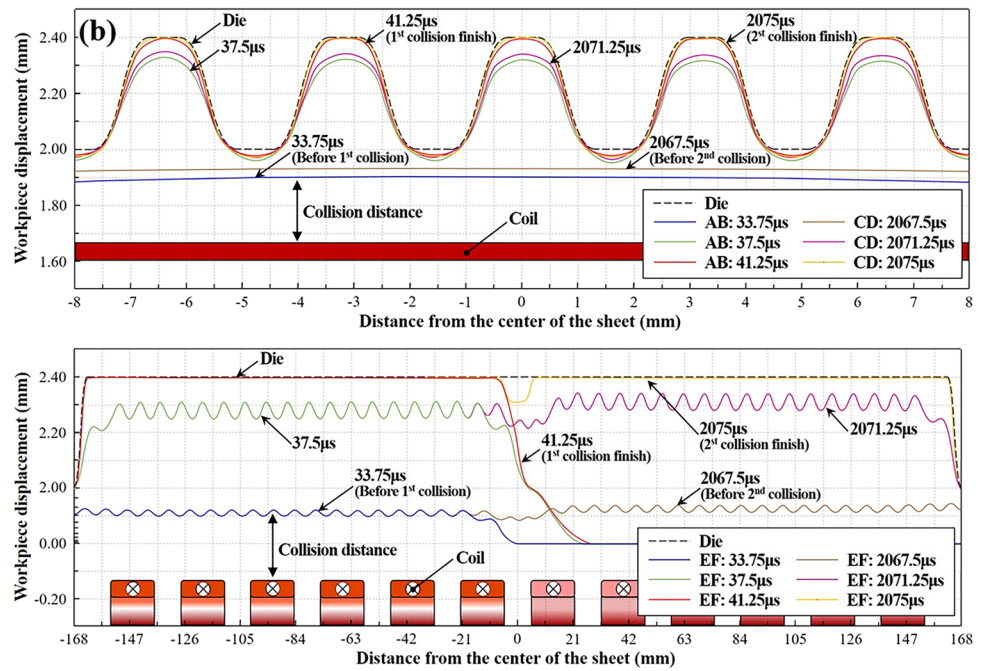

Fig. 26 Nephogram of deformation velocity variation on the titanium plate

to other locations, indicating that the corner region R of the mold is the most susceptible to thickness reduction. To analyze the deformation characteristics of the titanium plate under the UP-EMIF process, stress analysis of the plate is conducted on small elements in the bulging region A, corner region r, sidewall region B, corner region R, and ridge region C during the forming process, as depicted in Fig. 31. The deformation process of the titanium plate consists of two stages: free bulging and die conforming. The bulging region A, sidewall region B, and ridge region C are always subjected to biaxial tensile stress during the deformation process, which belongs to elongation-type deformation. Due to the biaxial frictional forces exerted by the driver sheet and the mold, the ridge region C experiences higher friction compared to the bulging region A, which only experiences unilateral friction in the first stage, resulting in more severe thickness reduction. Compared to the inner wall of the corner region r, the outer wall of the corner region R experiences higher bending-induced compressive stress and is consistently subjected to biaxial tensile stress and uniaxial compressive stress, resulting in more severe thickness reduction.

Fig. 27 Velocity vector distribution of the titanium plate at different time points: **a** 26.25 μs; **b** 33.75 μs; **c** 37.5 μs; **d** 41.25 μs; **e** 502.5 μs; **f** 2075 μs
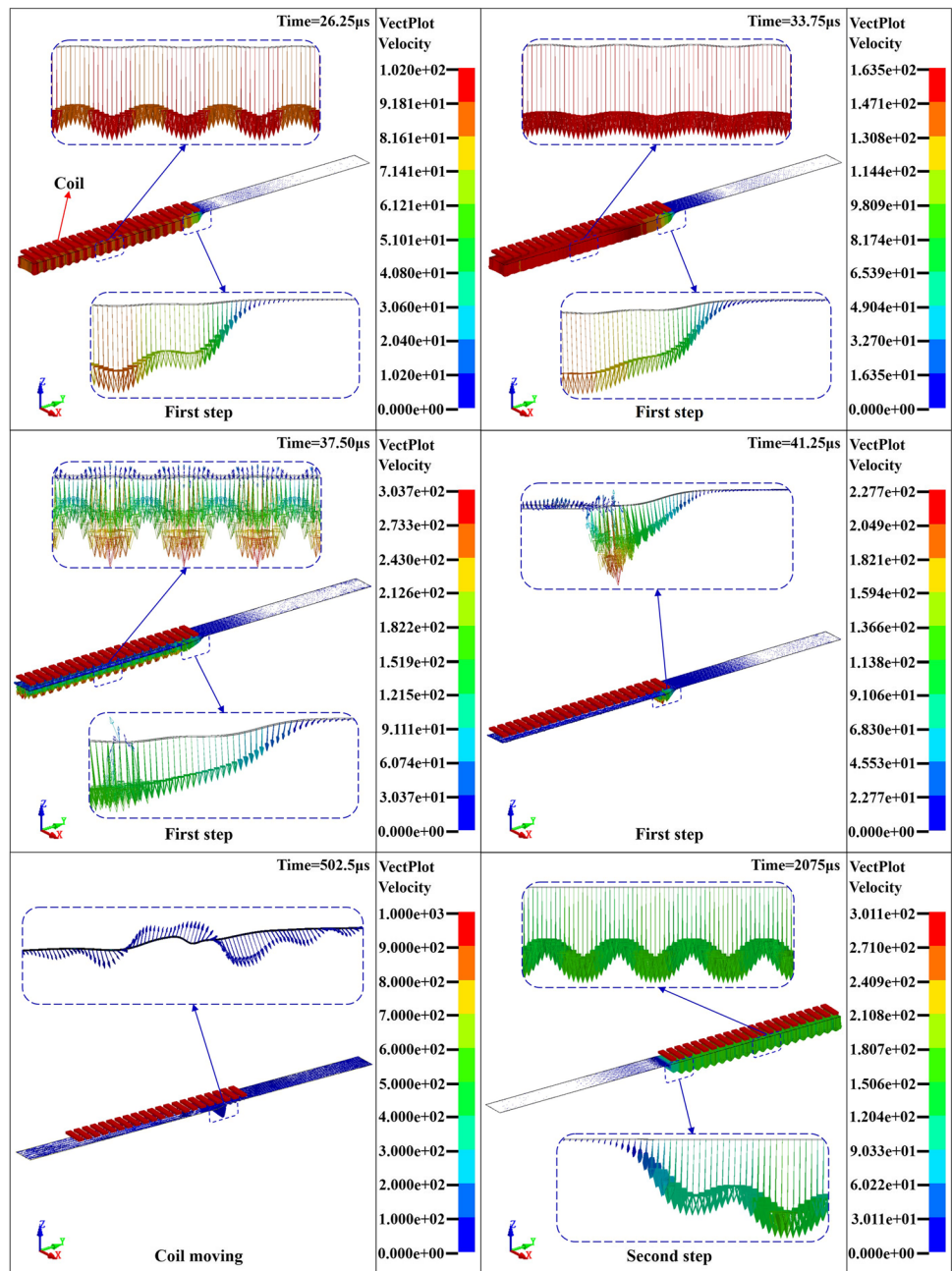
5.3 Profile dimensional changes

To compare the differences between UP-EMIF and traditional QS-DRPF processes, TA1 titanium BPP was prepared using a 2-mm acceleration distance and a 0.3-mm-thick Cu110 driver sheet. The low-voltage three-stage incremental forming method was employed with a 9 kV voltage, and the rubber pad forming method was carried out with 80 kN and 120 kN loads at a strain rate of $(6\sim7) \times 10 \text{ s}^{-4}$. Fig. 32 shows the titanium BPP prepared by UP-EMIF, while Fig. 33 shows the titanium BPP prepared by traditional QS-DRPF technique. The cross-sections of the BPP flow channels in

Figs. 33 and 34 were observed using a stereomicroscope, and the thicknesses of the expansion zone, fillet zone, sidewall zone, and ridge zone (1–9) were measured, as shown in Fig. 34. The cross-section thickness of the BPP under multi-stage UP-EMIF is more uniform and smooth, with a maximum thinning rate of 18.2%. However, the BPP cross-section obtained by QS-DRPF exhibits significant thinning at the 4th and 6th fillet zones, with a maximum thinning rate of 25.2%, approaching the fracture limit.

Extract segments of channels from Figs. 33 and 34, select 20 channels, and scan the profiles along the TD direction using a comprehensive measurement system for surface
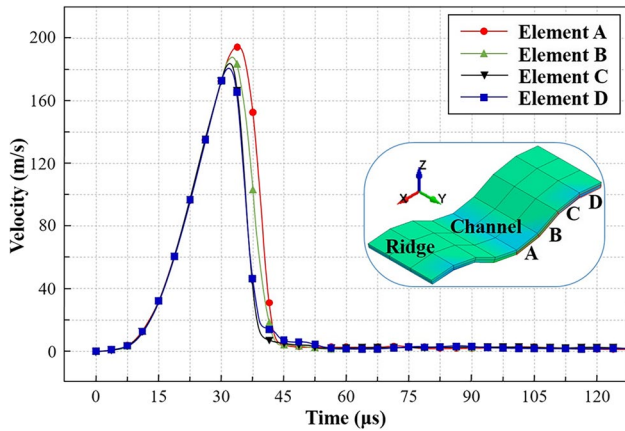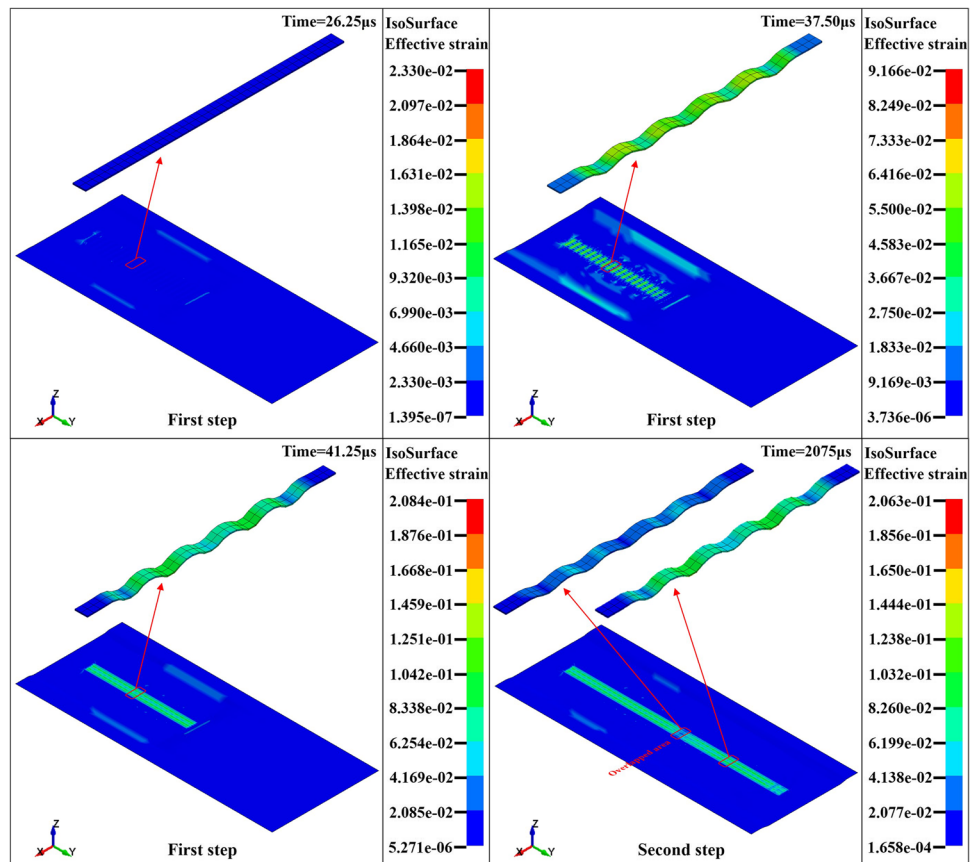
Fig. 28 Velocity-time curve of typical element in the single channel region α

5.4 Microstructural analysis

The formation of twinning can significantly reduce the average free path of dislocations, increase strain hardening rate, thus significantly delaying the occurrence of necking, and promoting uniform deformation of the material. High-temperature X-ray diffraction (XRD) and electron back scatter diffraction (EBSD) techniques were used to test the impact area of QS-DRPF and three-pass UP-EMIF BPPs. Fig. 37 shows the XRD patterns of the surface microstructure of TA1 titanium plate before and after forming. The intensities of the two-phase diffraction peaks are reduced in both processes, and the surface lattice of the forming region undergoes severe distortion and deformation. Fig. 38 shows the IPF and pole figures of TA1 titanium plate under the two processes. Both TA1 titanium plates exhibit obvious <0001> basal texture, and there are some small bamboo leaf–shaped deformed twins inside equiaxed grains. The twinning density of TA1 titanium plate after QS-DRPF is about 1.63%, while the twinning density of TA1 titanium plate after three-pass UP-EMIF is about 6.84%. Compared to QS-DRPF, deformation twinning under three-pass UP-EMIF can accommodate more strain. In addition, the twinning-induced plasticity effect (TWIP) [36, 37] is enhanced under three-pass UP-EMIF, resulting in a higher uniform
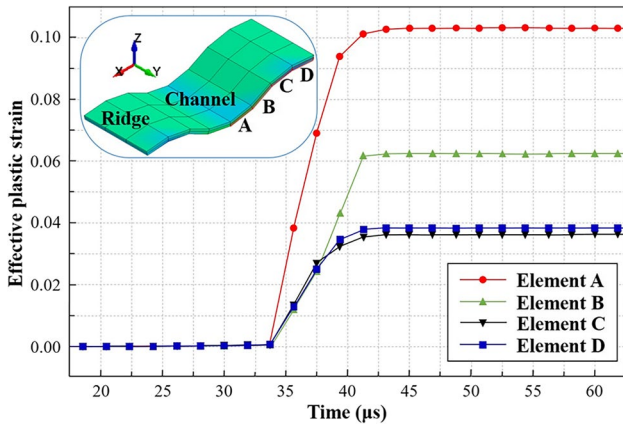
profile. Fig. 35 shows the depth of each channel along the TD direction. Fig. 36 shows the profiles of 20 channels along the TD direction on the BPP surface. It can be observed from the results that the depths of the channels fluctuate between 0.38 and 0.39 mm, with a fluctuation rate of less than ±2.17%. The channel filling rate is higher than 96.3%, which is sufficient to meet industrial requirements.

Fig. 29 Equivalent strain nephogram of the titanium plate at different time points: **a** 26.25 μs; **b** 37.5 μs; **c** 41.25 μs; **d** 2075 μs

Fig. 30 Variation of equivalent strain with time for typical element in the single-channel region α

elongation rate and an improvement in ultimate strain. The average grain sizes of TA1 titanium plates under the two processes are 10.9 μm and 8.6 μm, respectively, as shown in Fig. 39, reflecting the grain refinement phenomenon of the material at high strain rates.

5.5 Acceleration distance

Figure 40 illustrates the principle of sheet metal forming. The titanium plate to be formed achieves the desired shape by high-speed collision with the mold at an acceleration distance *d*. According to Golowin et al. [38], during the high-speed collision between the workpiece and the mold,

the velocity of the workpiece is converted into the impact pressure exerted by the mold on the workpiece, as shown in Eq. (2).

$$P_{impact} = \frac{\rho_1 \rho_2 C_1 C_2}{\rho_1 C_1 + \rho_2 C_2} V_i \tag{2}$$

Here, ρ_1 and ρ_2 represent the mass densities of the mold and workpiece, and C_1 and C_2 represent the longitudinal wave velocities of the mold and workpiece. The forming effect of the workpiece is closely related to the impact pressure during the collision.

When using discharge capacitance of 100 μF and discharge voltage of 15 kV, with acceleration distances of 0 mm, 2 mm, and 4 mm, the displacement of the bottom element of the flow channel on paths ab and cd over time is obtained through simulation, as shown in Fig. 41. A slight oscillation rebound phenomenon occurs when the acceleration distance is 2 mm, which can be counteracted by multiple discharges. Fig. 42 shows the surface morphology of titanium BPP with acceleration distances of 2 mm and 4 mm under a discharge voltage of 9 kV. When the acceleration distance is 4 mm, the formed titanium BPP surface exhibits protrusions caused by rebound. Wu et al. [16] pointed out that when the distance between the workpiece and the mold is within 4 mm, the workpiece can inherit the uniform speed of the driver sheet. Therefore, the acceleration distance should be controlled to around 2 mm to ensure the workpiece speed while minimizing workpiece oscillation.

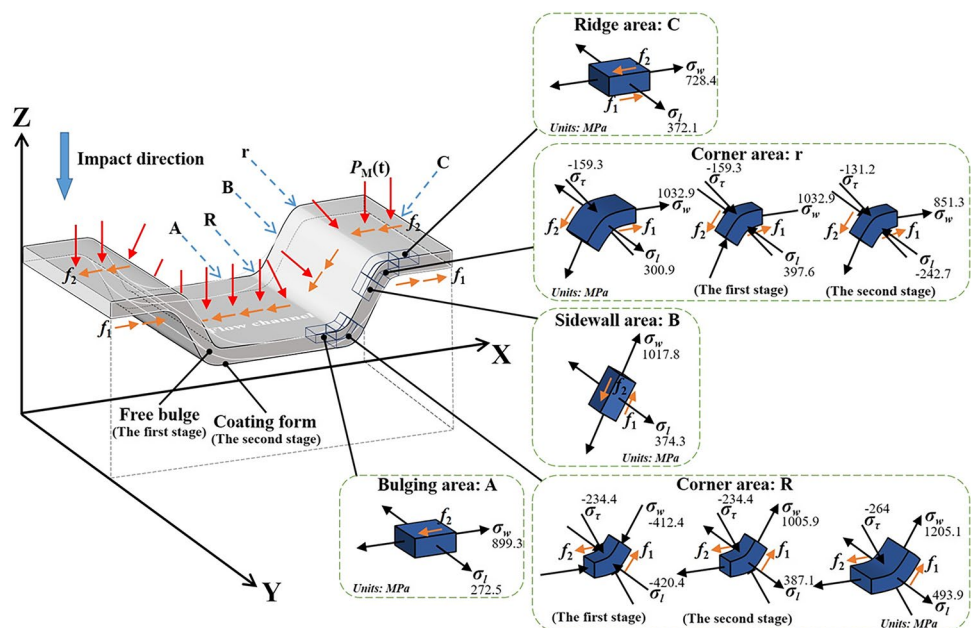**Fig. 31** Analysis of stress in the titanium plate during the forming process

Fig. 32 Titanium bipolar plates fabricated by 0.3-mm-thick Cu110 driver sheet under three 9 kV continuous discharges and 2-mm acceleration distance
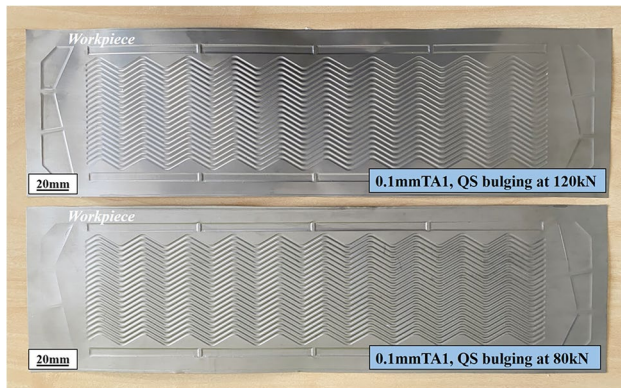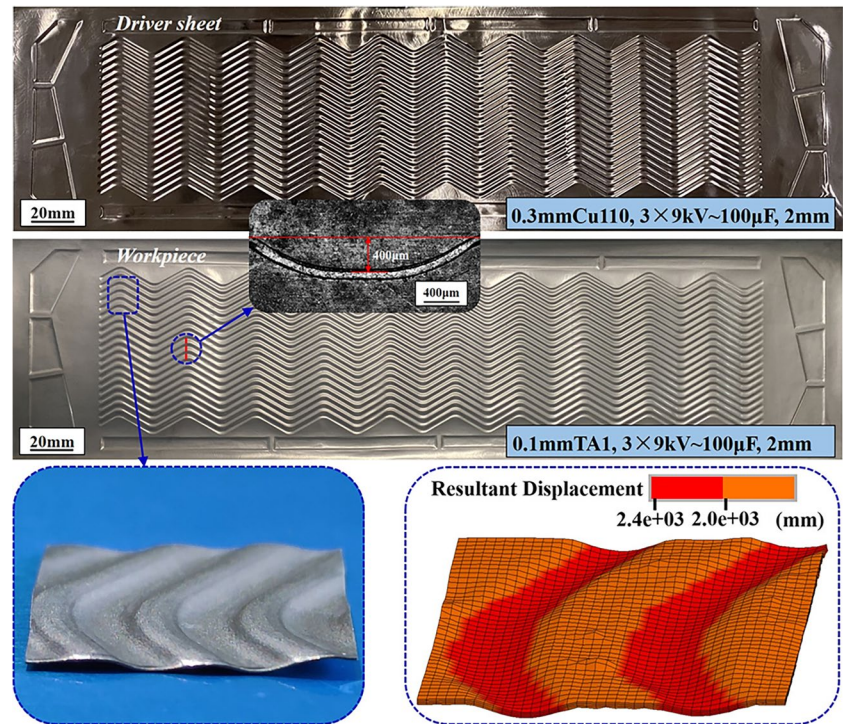

Fig. 33 Titanium bipolar plates fabricated by rubber pad forming under 80 kN and 120 kN load

5.6 Discharge parameters

Under the condition of fixed energy storage equipment, the discharge parameters are mainly adjusted by changing the discharge voltage and discharge frequency. Increasing the voltage is the most intuitive method to improve the forming ability, but it also imposes higher requirements on the coil strength and circuit insulation level [17]. Fig. 43 shows the

TA1 titanium BPP formed by discharging at 6 kV, 9 kV, 12 kV, and 15 kV, with a discharge capacitance of 100 µF and an acceleration distance of 2 mm, driven by a 0.2-mm-thick driver sheet. As the discharge voltage increases, the depth of the BPP channel gradually increases, indicating that increasing the voltage can significantly improve the channel depth. However, when the discharge voltage is 6 kV or 9 kV, some contact gaps between the outer channel and the driver sheet cause severe arcing, accompanied by spot welding phenomena, as shown in Fig. 44a and c. According to the work reported by Kamal [21], the current approach to avoid arcing mainly involves the use of a flexible layer between the metal sheet and the mold, maintaining good cleanliness of the contact surface, and higher contact load. In this study, a method of coating the bottom of the outer channel with isotropic conductive adhesive (ICA) is used, and the migration of ICA is utilized to fill the gaps, as shown in Fig. 44b and d, significantly improving the arcing issue.

High voltage can cause severe arcing issues, while low voltage can result in insufficient forming energy, making it impossible to achieve BPP forming. Simulation of the incremental forming of titanium BPP with 9 kV and three consecutive discharges, with a discharge capacitance of 100 µF and an acceleration distance of 2 mm, yields displacement nephogram of the flow channels corresponding to five array channels, as shown in Fig. 45a. Typical bottom elements A
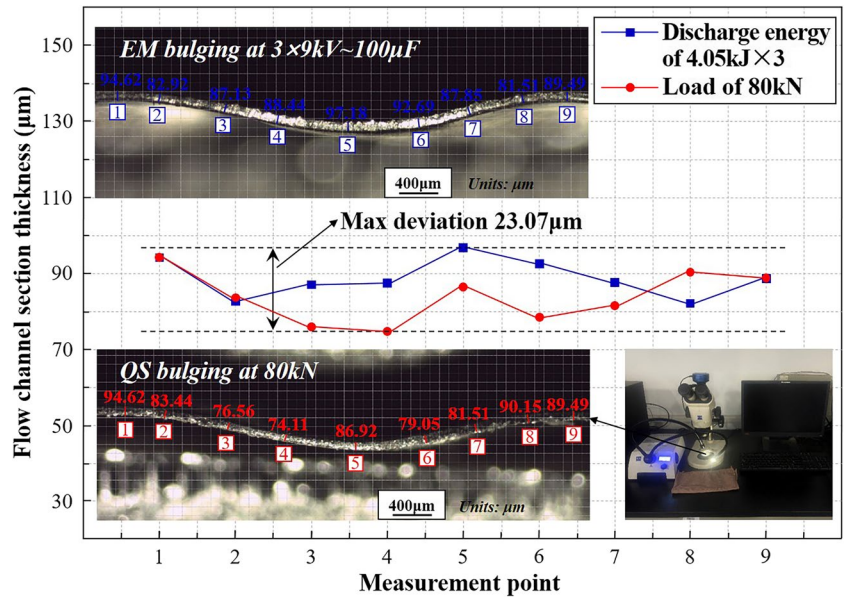
Fig. 34 Variation in channel cross-sectional thickness

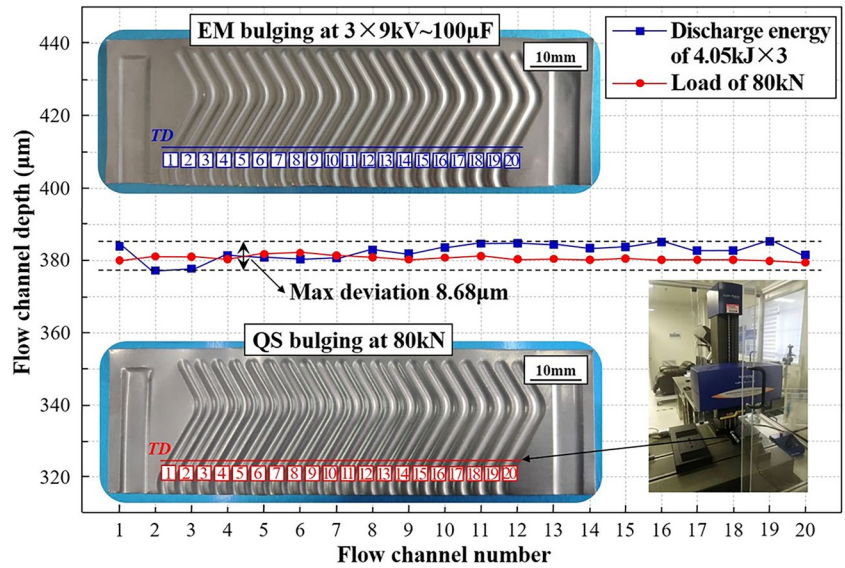**Fig. 35** Depths of channel in the TD direction of BPP

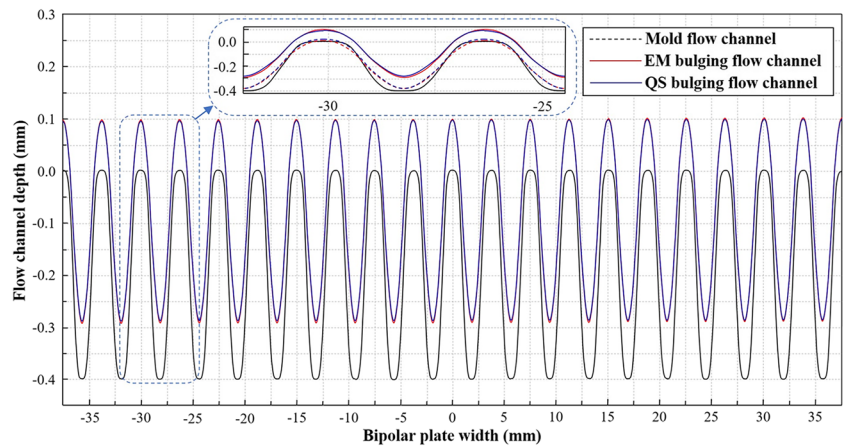**Fig. 36** Comparison of BPP and mold channel profile

Fig. 37 XRD patterns of surface microstructure of TA1 titanium plate before and after forming
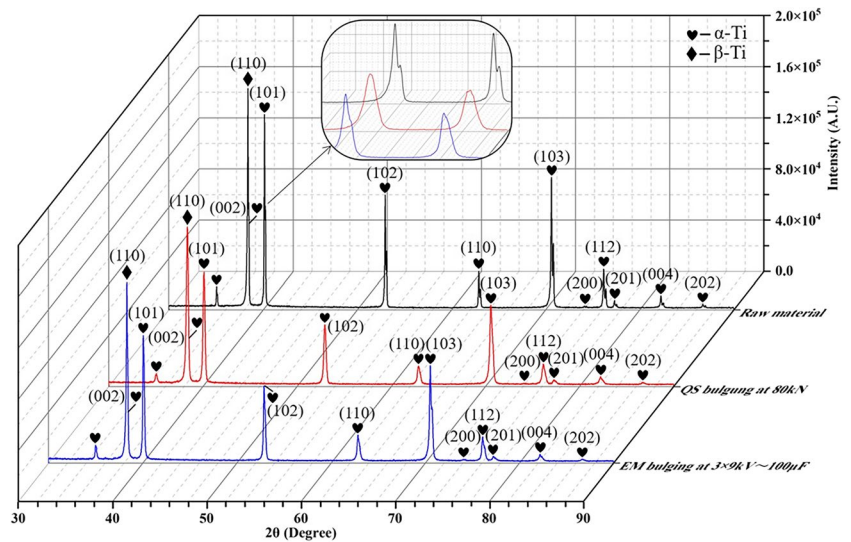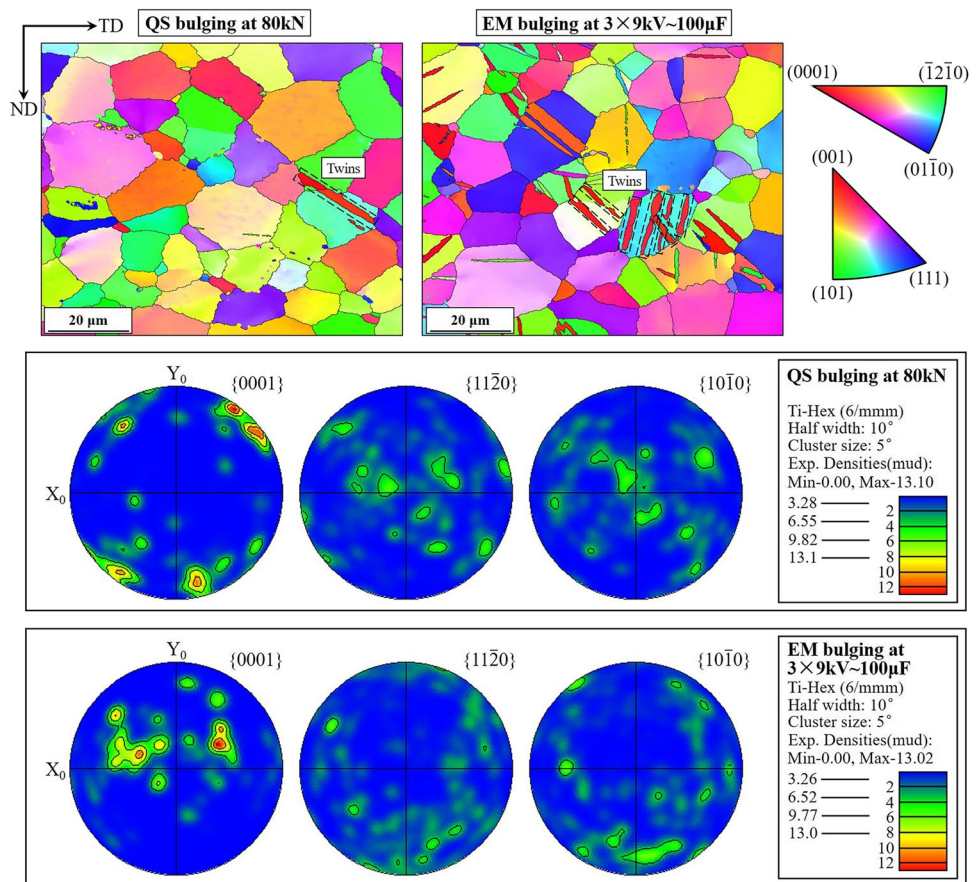

Fig. 38 EBSD analysis of workpieces under two different processes: **a** IPF map under QS-DRPF conditions; **b** IPF map under 9 kV three pass UP-EMIF conditions; **c** pole figure under QS-DRPF conditions; **d** pole figure under 9 kV three pass UP-EMIF conditions

and B of the flow channels in the two discharge regions are selected, and their displacements over time are shown in Fig. 45b. The two discharge regions undergo three acceleration processes, and the channel depths reach 0.13 mm, 0.31 mm, and 0.4 mm, respectively. Fig. 45c shows the depth of the workpiece channels for 9 kV and three consecutive discharges, as well as for a single discharge at 15 kV. The forming effect achieved with 9 kV and three consecutive discharges is consistent with the experimental results, realizing the formation of BPP.

Fig. 39 Grain size distribution under two different processes. **a** QS-DRPF conditions; **b** 9 kV three pass UP-EMIF conditions
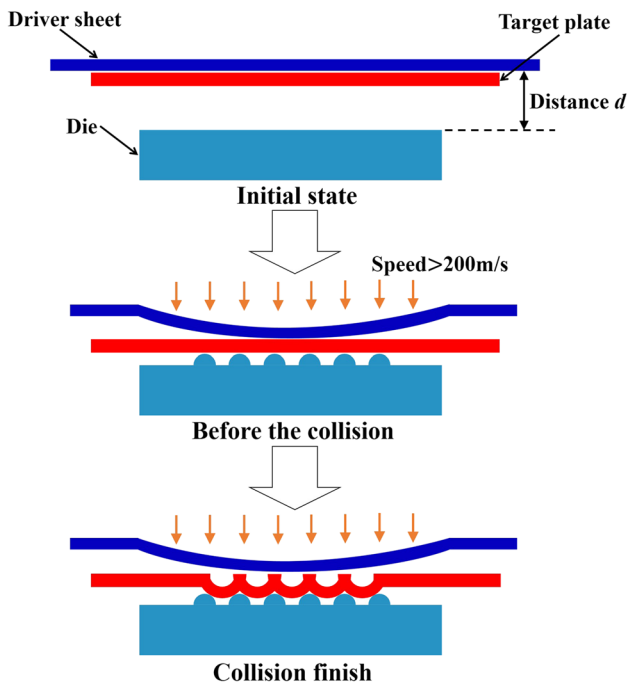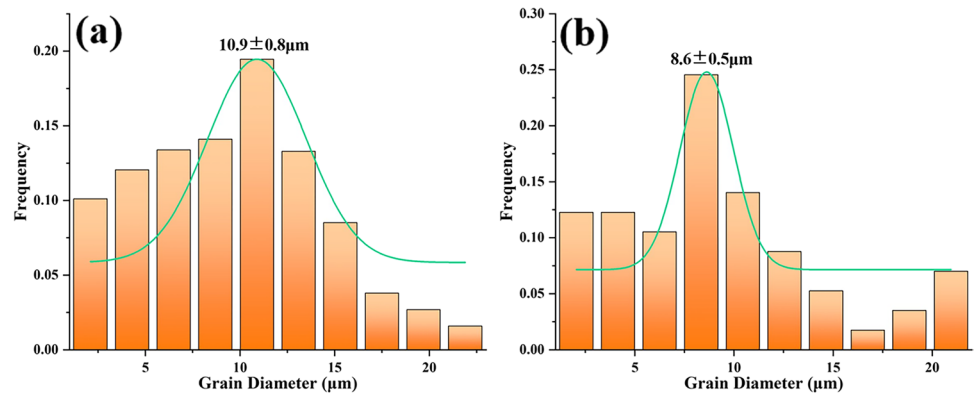

Fig. 40 Schematic diagram of the forming principle of sheet

Fig. 41 Oscillation process of the workpiece under different acceleration distances

5.7 Coil overlap ratio

To investigate the influence of coil overlap ratio on the uniformity of plate deformation, simulations were conducted with coil overlap ratios of 0%, 5%, and 15% under discharge capacitance of 100 μF and discharge voltage of 15 kV. The displacement of the workpiece in the RD direction in the coil overlap region was obtained as shown in Fig. 46. According to the industrial requirement of ±2.5% fluctuation in the flow channel [39], a criterion for the uniformity of plate deformation in the RD direction was set. After the plate
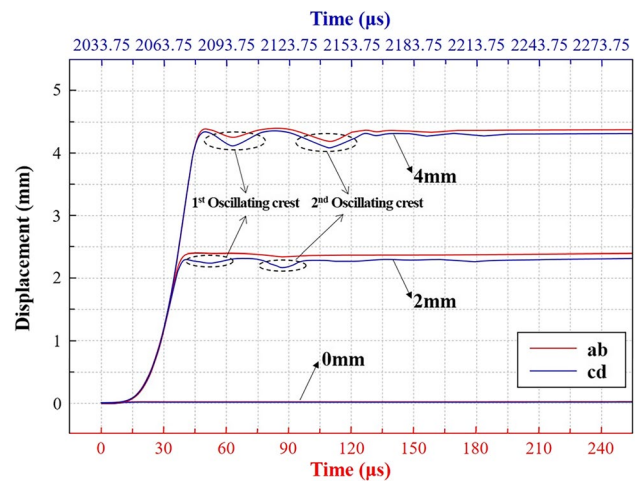
deformation, the maximum flow channel depth D_{max} and the minimum flow channel depth D_{min} on the lower surface were extracted, as shown in Table 5. If $|D_{max} - D_{min}| \leq 0.025|D_{max}|$, then the deformation is considered uniform. Fig. 47 shows the forming results with gradually increasing coil overlap ratios of 3 steps and 9 kV under discharge capacitance of 100 μF, acceleration distance of 2 mm, and driving with a 0.3-mm-thick Cu110 driver sheet. Due to the influence of coil end effects, the flow channel depth near the overlap line is significantly insufficient when the coils overlap exactly. However, when the coil overlap ratio is 15%, the coil end effects are eliminated, and TA1 titanium BPP parts with uniform flow channel formation are prepared, which is consistent with the simulation conclusion. The flow channel depth was measured at 5 points along the RD direction in both the overlapping and non-overlapping regions of

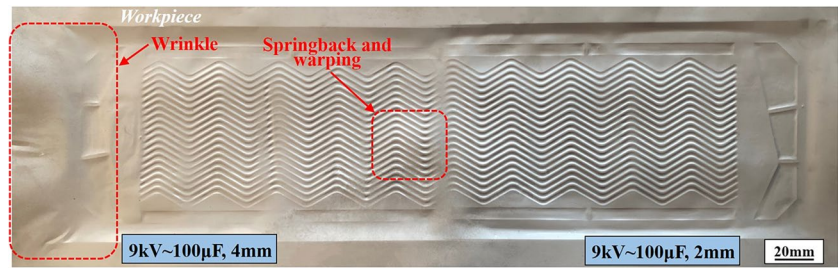**Fig. 42** TA1 titanium BPP obtained under different acceleration distances

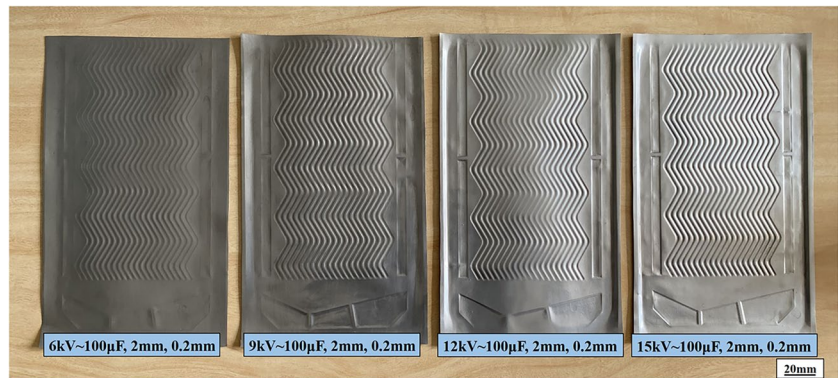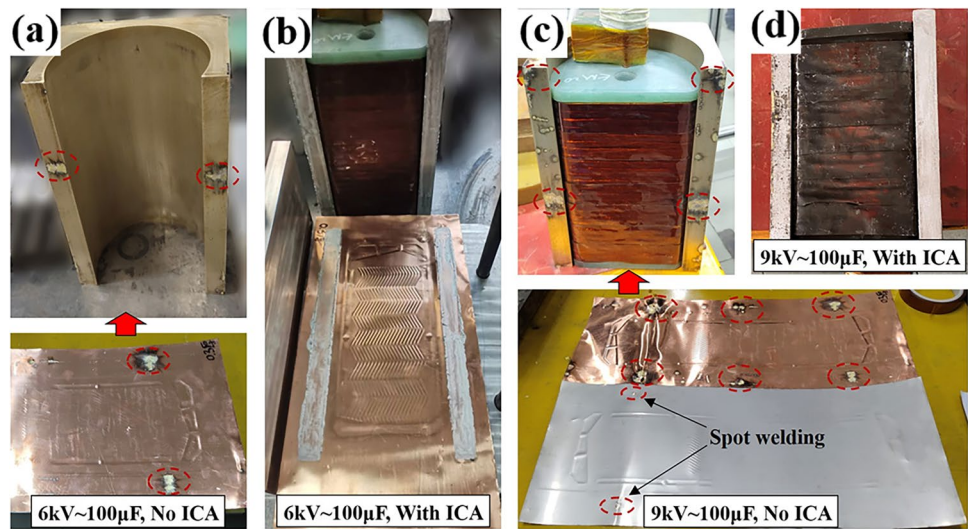**Fig. 43** TA1 titanium BPP formed under different discharge voltages

Fig. 44 Arc phenomena between the outer channel and the driver sheet under different discharge voltages: **a** uncoated ICA at 6 kV discharge voltage; **b** ICA coated at 6 kV discharge voltage; **c** uncoated ICA at 9 kV discharge voltage; **d** ICA coated at 9 kV discharge voltage

the workpiece using a spiral micrometer, and the average value was obtained. The final flow channel depth is shown in Fig. 48. The simulation results are generally higher than the experimental results numerically. As the coil overlap ratio increases, the two results gradually approach the flow channel depth in the non-overlapping region, and their errors gradually decrease. Therefore, the UP-EMIF process can form BPPs that meet the criterion of uniform deformation.

6 Conclusion

In this study, the forming process of automotive titanium BPP using UP-EMIF with designed arc spiral coils was analyzed in depth, and large-sized TA1 titanium BPP with sufficient channel depth, filling ratio, low channel fluctuation, and thinning rate was successfully fabricated. The following conclusions were drawn:
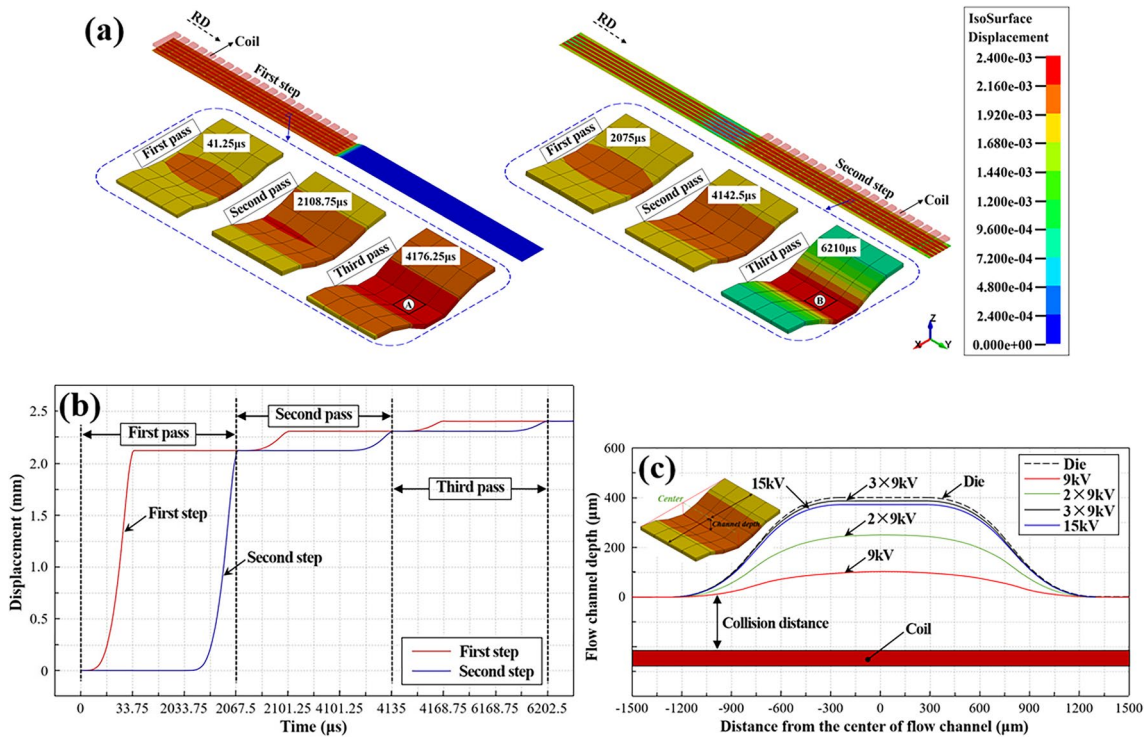
Fig. 45 Channel depth of two discharge regions under 9 kV three-step incremental discharge: **a** channel displacement nephogram; **b** displacement-time curve of bottom element of the channel; **c** channel depth of workpiece under 9 kV three-step and 15 kV single-step discharge
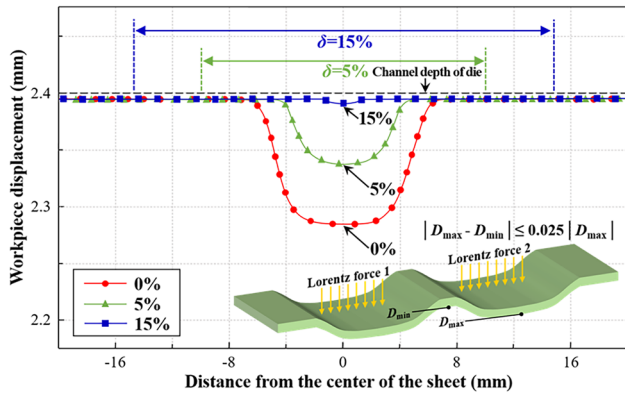

Fig. 46 Workpiece displacement in the coil overlap region along the RD direction under different coil overlap ratios

Table 5 Determination results of uniformity criteria

Overlap ratio (%)	D_{max} (μm)	D_{min} (μm)	$(D_{max}-D_{min})/D_{max}$	Satisfying uniform deformation
0	394.25	284.25	0.280	No
5	394.51	337.48	0.145	No
15	394.88	390.34	0.011	Yes

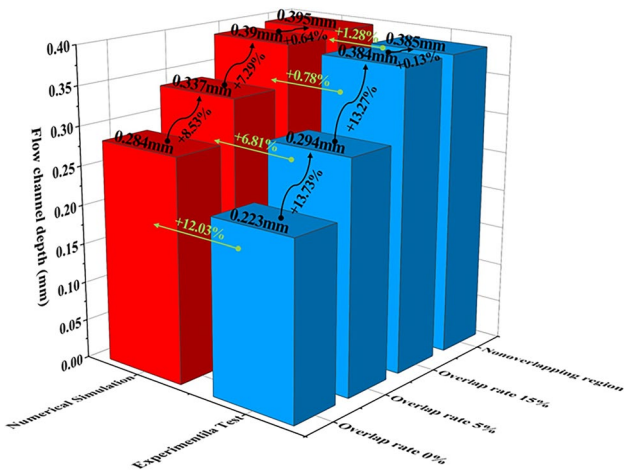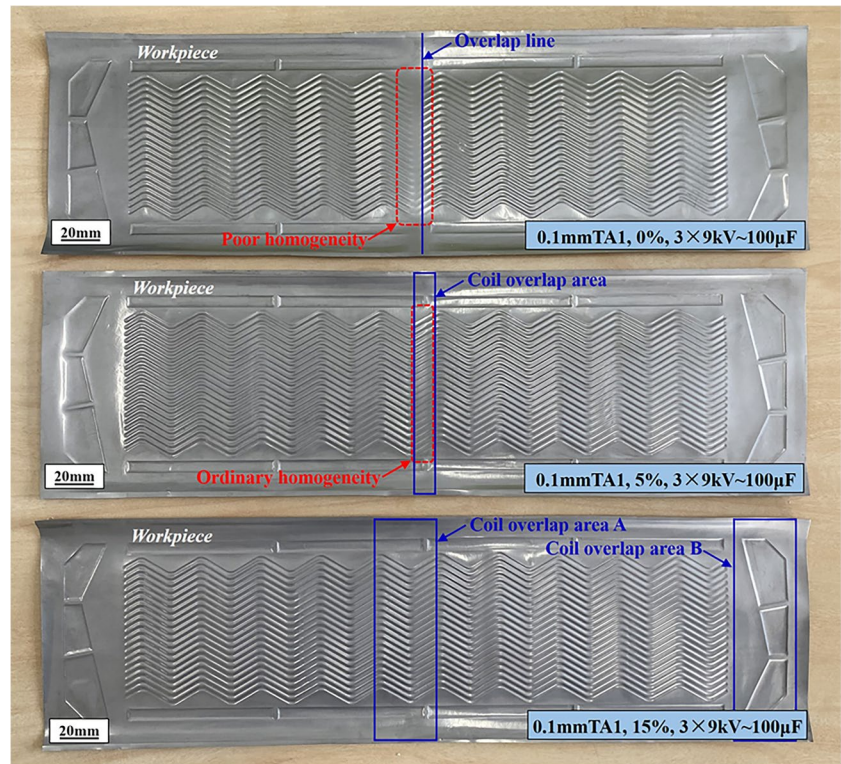**Fig. 47** TA1 titanium BPP formed under different coil overlap ratios

Fig. 48 Comparative analysis of channel depth in the overlapping region of BPP under various coil overlap ratios

(1) The electromagnetic force acting on the arc UPC under compression does not cause coil failure. The electromagnetic force on the outer channel tends to repel the driver sheet, which is the fundamental cause of arc generation. Coating ICA can significantly improve the arc problem and increase the voltage margin to 9 kV. The electromagnetic force on the driver sheet changes from a wave-like pattern to a uniform distribution, providing uniform pressure for the formed BPP.

(2) With a discharge energy of 11.25 kJ and an acceleration distance of 2 mm, the titanium plate can be accelerated to 195 m/s. The formed BPP has a channel depth of 0.4 mm and a channel depth-to-width ratio of 0.53. The highest equivalent strain occurs in the corner R region of the BPP, making it most susceptible to wall thinning.

(3) Compared to traditional QS-DRPF, UP-EMIF can significantly reduce the thinning rate of BPP, with a maximum thinning rate of 18.2%, while increasing the channel filling ratio, with a maximum filling ratio of 96.3%, and improving the uniformity of channel depth, with a channel fluctuation rate less than $\pm 2.17\%$.

(4) By controlling the acceleration distance to approximately 2 mm, the workpiece can maintain the uniform velocity of the driver sheet and reduce workpiece oscillation. According to the uniformity criterion $|D_{max} - D_{min}| \leq 0.025|D_{max}|$, when the coil overlap rate reaches 15%, the BPP satisfies the condition of uniform deformation.

Data availability This is not applicable.

Code availability This is not applicable.

Declarations

Ethics approval This is not applicable.

Consent to participate This is not applicable.

Consent to publication This is not applicable.

Conflict of interest The authors declare no competing interests.

References

1. Wang SH, Peng J, Lui WB (2006) Surface modification and development of titanium bipolar plates for PEM fuel cells. J Power Sources 160:485–489
2. Wang SH, Peng J, Lui WB, Zhang JS (2006) Performance of the gold-plated titanium bipolar plates for the light weight PEM fuel cells. J Power Sources 162:486–491
3. Selahattin C, Bora T, Ugur A, Mikail Y (2022) Development of titanium bipolar plates fabricated by additive manufacturing for PEM fuel cells in electric vehicles. Int J Hydrogen Energ 47:37956–37966
4. Chen FK, Chiu KH (2005) Stamping formability of pure titanium plates. J Mater Process Tech 170:181–186
5. Vahid M, Hossein TG, Vali A, Majid E (2021) Fracture prediction in the stamping of titanium bipolar plate for PEM fuel cells. Int J Hydrogen Energ 46:5729–5739
6. Xu ZT, Li ZP, Zhang R, Jiang TH, Peng LF (2021) Fabrication of micro channels for titanium PEMFC bipolar plates by multi-stage forming process. Int J Hydrogen Energ 46:11092–11103
7. Mahabunphachai S, Cora ÖN, Koç M (2010) Effect of manufacturing processes on formability and surface topography of proton exchange membrane fuel cell metallic bipolar plates. J Power Sources 195:5269–5277
8. Kim MJ, Jin CK, Kang CG (2015) The effect of different forming parameters on the depth of bipolar-plate channels in static-and dynamic-load stamping. P I Mech Eng B-J Eng 229:1976–1983
9. Jin CK, Jeong MG, Kang CG (2014) Fabrication of titanium bipolar plates by rubber forming and performance of single cell using TiN-coated titanium bipolar plates. Int J Hydrogen Energ 39:21480–21488
10. Lee KH, Jin CK, Kang CG, Seo HY, Kim JD (2015) Fabrication of titanium bipolar plates by rubber forming process and evaluation characteristics of TiN coated titanium bipolar plates. Fuel Cells 15:170–177
11. Psyk V, Risch D, Kinsey BL, Tekkaya AE, Kleiner M (2011) Electromagnetic forming–a review. J Mater Process Technol 211:787–829
12. Li FQ, Mo JH, Li JJ, Zhou HY, Huang L (2013) Study on the driver plate for electromagnetic forming of titanium alloy Ti-6Al-4V. Int J Adv Manuf Technol 69:127–137
13. Li FQ, Zhao J, Mo JH, Li JJ, Huang L (2017) Comparative study of the microstructure of Ti-6Al-4V titanium alloy sheets under quasi-static and high-velocity bulging. J Mech Sci Technol 31:1349–1356
14. Kamal M, Daehn GS (2007) A uniform pressure electromagnetic actuator for forming flat sheets. J Manuf Sci Eng 129:369–379
15. Wang HM, Wang YL (2019) Investigation of bipolar plate forming with various die configurations by magnetic pulse method. Metals 9:453
16. Wu ZL, Cao QL, Fu JY, Li ZZ, Wan Y, Chen Q (2020) An inner-field uniform pressure actuator with high performance and its application to titanium bipolar plate forming. Int J Mach Tool Manu 155:103570
17. Dong PX, Li ZZ, Feng S, Wu ZL, Cao QL, Li L (2021) Fabrication of titanium bipolar plates for proton exchange membrane fuel cells by uniform pressure electromagnetic forming. Int J Hydrogen Energ 46:38768–38781
18. Zhu CX, Xu J, Yu HP, Shan D, Guo B (2022) Hybrid forming process combining electromagnetic and quasi-static forming of ultra-thin titanium plates: formability and mechanism. Int J Mach Tool Manu 180:103929
19. Cui XH, Qiu DY, Jiang L, Yu HL, Du ZH, Xiao A (2019) Electromagnetic sheet forming by uniform pressure using flat spiral coil. Materials 12:1963
20. Li ZZ, Han XT, Cao QL, Xiong Q, Li L (2016) Design, fabrication, and test of a high-strength uniform pressure actuator. IEEE T Appl Supercon 26:3700905
21. Kamal M (2005) A uniform pressure electromagnetic actuator for forming flat sheets. The Ohio State University
22. Kristin E, Banik BS (2008) Factors effecting electromagnetic flat sheet forming using the uniform pressure coil. The Ohio State University
23. Imbert J, Winkler S, Worswick MJ, Oliveira DA, Golovashchenko SF (2004) Numerical study of damage evolution and failure in an electromagnetic corner fill operation. In: Proceedings of the 8th International Conference on Numerical Methods in Industrial Forming Processes, AIP Conference Proceedings, Columbus, Ohio(USA) 712: 1833-1838
24. Oliveira DA, Worswick M (2003) Electromagnetic forming of aluminium alloy sheet. J Phys IV 110:293–298
25. Yu HP, Li CF, Deng JH (2009) Sequential coupling simulation for electromagnetic–mechanical tube compression by finite element analysis. J Mater Process Tech 209:707–713
26. Cao QL, Li L, Lai ZP, Zhou ZY, Xiong Q, Zhang X (2014) Dynamic analysis of electromagnetic sheet metal forming process using finite element method. Int J Adv Manuf Technol 74:361–368
27. Xu JR, Cui JJ, Lin QQ, Li YR (2015) Magnetic pulse forming of AZ31 magnesium alloy shell by uniform pressure coil at room temperature. Int J Adv Manuf Technol 77:289–304
28. Cui XH, Mo JH, Xiao SJ, Du EH (2011) Magnetic force distribution and deformation law of sheet using uniform pressure electromagnetic actuator. T Nonferr Metal Soc 21:2484–2489
29. Kinsey B, Zhang S, Korkolis YP (2018) Semi-analytical modelling with numerical and experimental validation of electromagnetic forming using a uniform pressure actuator. CIRP Annals 67:285–288
30. Cui XH, Mo JH, Li JJ, Zhao J, Xiao SJ (2012) Produce a large aluminum alloy sheet metal using electromagnetic-incremental(EM-IF) forming method: experiment and numerical simulation. In: 5th International Conference on High Speed Forming. Dortmund, Germany, pp 59–70

31. Cui XH, Li JJ, Mo JH, Fang JX, Zhu YT, Zhong K (2015) Investigation of large sheet deformation process in electromagnetic incremental forming. Mater Design 76:86–96

32. Cui XH, Mo JH, Li JJ, Xiao XT, Zhou B, Fang JX (2016) Large-scale sheet deformation process by electromagnetic incremental forming combined with stretch forming. J Mater Process Technol 237:139–154

33. Cui XH, Du ZH, Xiao A, Yan ZQ, Qiu DY, Yu HL (2021) Electromagnetic partitioning forming and springback control in the fabrication of curved parts. J Mater Process Technol 288:116889

34. Poizat C, Campagne L, Daridon L, Ahzi S, Husson C, Merle L (2005) Modeling and simulation of thin sheet blanking using damage and rupture criteria. Int J Form Processes 8:29–47

35. Deng JH, Tang C, Li CF, Yu HP, Jiang HW (2012) Determination of TA1 constitutive model. J Plas Eng 19:114–117 (In Chinese)

36. De Cooman BC, Kwon O, Chin KG (2012) State-of-the-knowledge on TWIP steel. Mater Sci Technol 28:513–527

37. De Cooman BC, Estrin Y, Kim SK (2018) Twinning-induced plasticity (TWIP) steels. Acta Mater 142:283–362

38. Golowin S, Kamal M, Shang JH, Portier J, Din A, Daehn GS (2007) Application of a uniform pressure actuator for electromagnetic processing of sheet metal. J Mater Eng Perform 16:455–460

39. Li ZZ (2020) A uniform pressure electromagnetic forming method and process on titanium bipolar plate of hydrogen fuel cell. Huazhong University of Science and Technology